



37 **Abstract (180 words)**

38 Our current understanding of the pathophysiology of human pulmonary TB is limited by the paucity  
39 of human TB lung tissue for study and reliance on 2D analytical methods. Here, to overcome the  
40 limitations of conventional 2D histopathology, we used high-resolution 3D X-ray imaging  
41 ( $\mu$ CT/nCT) to characterize necrotic lesions within human tuberculous lung tissues in relation to the  
42 airways and vasculature. We observed marked heterogeneity in the 3D structure and volume of  
43 lesions. Also, 3D imaging of large human TB lung sections provides unanticipated new insight into  
44 the spatial organization of TB lesions in relation to airways and the vascular system. Contrary to  
45 the current dogma depicting granulomas as simple spherical structures, we show that TB lesions  
46 exhibit complex, cylindrical, branched-type morphologies, which are connected to, and shaped by,  
47 the small airways. Our results highlight the likelihood that a single structurally complex lesion  
48 could be wrongly viewed as multiple independent lesions when evaluated in 2D. These findings  
49 have strong implications for understanding the pathophysiology and evolution of TB disease and  
50 suggest that aerosolized drug delivery strategies for TB should be reconsidered.

51

52 **Introduction**

53 Tuberculosis (TB) is a global infectious disease caused by the bacterium *Mycobacterium*  
54 *tuberculosis* (*Mtb*). Histopathological analysis was a mainstay for the investigation of TB disease  
55 throughout the 1940s<sup>1</sup> and 1950s<sup>2</sup> when post-mortem and resected human lung tissues were  
56 routinely available. These pioneering studies have strongly influenced our current understanding  
57 of the spectrum of tuberculous lesions, morphology and pathology.

58 The prevailing dogma in the TB field is that TB granulomas form spherical or ovoid  
59 structures within the parenchyma<sup>3-11</sup>. However, this assumption is not always supported by  
60 experimental evidence. Further, remarkably little is known about the structure of the caseous  
61 granuloma, the distinctive feature of infection by *Mtb* in humans. Hence, a deeper understanding  
62 of the human TB granuloma is urgently needed to more accurately inform preventive and  
63 therapeutic TB strategies.

64 The ability to examine pathological TB structures within large tissues in 3D could allow  
65 identification of disease-specific features and improve diagnosis. Hence, it is reasonable to  
66 speculate that the limitations of conventional histological analysis have begun to hinder more  
67 detailed examination of human TB pathophysiology in the current antibiotic era, especially with the  
68 emergence of HIV. Other factors contributing to our limited understanding are the reliance on  
69 animal models which do not recapitulate human pulmonary TB phenotypes, and the paucity of  
70 routinely available resected human TB lung tissues<sup>12,13</sup>. Therefore, imaging approaches that  
71 provide high-resolution digital 3D imaging of TB lesions will allow comprehensive analysis of the  
72 complex 3D microanatomical features specific to pulmonary TB.

73 X-ray computed tomography (CT) is an invaluable imaging tool for nondestructive  
74 assessment of tissue in medical diagnosis<sup>14-16</sup>. High resolution micro-CT ( $\mu$ CT) is typically used  
75 for materials with high electron density and lends itself to *ex vivo* analysis of pathologies involving  
76 bone structure or calcium deposition<sup>17</sup>. Imaging of soft tissue can be improved by addition of  
77 electron-dense contrast agents (e.g., iodine, osmium, or tungsten) or using high-energy flux  
78 monochromatic x-rays generated by synchrotrons. To our knowledge, however, no study has  
79 reported the use of  $\mu$ CT to examine bacterial or viral disease in human lungs. While  $\mu$ CT is an  
80 experimental imaging modality, high-resolution computed X-ray tomography (HRCT) is often used

81 clinically to aid TB diagnosis<sup>18,19</sup>. Specifically, HRCT can detect phenotypes of *Mtb* infection such  
82 as bronchiectasis, cavity formation and tissue consolidation<sup>20</sup>. While HRCT is non-invasive, it  
83 suffers from lower resolution (~0.23-1.5 mm) and usually requires a contrast agent for imaging of  
84 homogeneous soft tissue<sup>21,22</sup>.

85 Here, we characterized the 3D environment of the human tuberculous lung *ex vivo*. We  
86 examined the 3D structure of TB granulomas, their spatial position relative to the airways and  
87 vasculature, and confirmed our findings using histopathology and immunohistochemistry. Overall,  
88 we demonstrate the utility of  $\mu$ CT for direct visualization of pulmonary TB in detail, thereby  
89 advancing our understanding of how *Mtb* causes destructive human TB.

90

## 91 **Results**

92

### 93 **$\mu$ CT characterization of the human TB granuloma**

94 In Durban, South Africa, *Mtb*-infected human lung tissues are routinely obtained following  
95 resection of irreversibly damaged lung regions exhibiting bronchiectasis and/or cavitary lung  
96 disease<sup>23,24</sup>. For this study, we analyzed formalin fixed (FF) lung specimens obtained from 17  
97 subjects (Table 1). Comprehensive sampling from different regions of each lung or lobe allowed  
98 us to evaluate microenvironments at different stages of tissue pathology. Gross architectural  
99 distortion with conspicuous upper lobe cavitation in a background of bronchiectasis, lung  
100 shrinkage, and fibrosis were noted in cut sections of several specimens. The specimens exhibited  
101 typical features of bronchiectasis and contained tubercles of varying size and shape.  
102 Representative sections of the cavitational and parenchymal abnormalities were used for imaging  
103 studies; see Table 1.

104 To improve the clinicopathological analysis of TB, we attempted to establish a  
105 correspondence between X-ray density and pathological features within lesions that permit 3D  
106 reconstruction. TB lesions have pathological features that can evolve over decades<sup>1,2</sup>. While  
107 these structures likely represent unique immunopathological microenvironments, their contribution  
108 to TB disease and persistence of *Mtb* is poorly understood. This partly due to the inability of 2D

109 histology to adequately characterize these deformities. We scanned a contrast-stained lung tissue  
110 sample (15 x 10 x 10 mm) with caseous necrosis (Figure 1A) at 12.0  $\mu\text{m}$  resolution (Figure 1B).  
111 Segmentation identified distinct regions that matched blood vessels and necrotic lesions. The  
112 identification of lesions and vasculature with  $\mu\text{CT}$  was confirmed by histology using H&E (Figure  
113 1C) and trichrome staining (Figure 1D), revealing several necrotic lesions and evidence of fibrosis.  
114 Inspection of the lesions revealed common electron density features, which we confirmed  
115 quantitatively by plotting relative X-ray attenuation (electron density) across representative  
116 sections (Figure 1E, F). First, the necrotic lesions are surrounded by a dark outer layer of CT  
117 intensity (Figure 1G-J) corresponding to lamellar fibrosis by H&E (Figure 1K-N) and trichrome  
118 staining (Figure 1O-R). Second, the necrotic region itself exhibits a light border (Figure 1G-J) that  
119 corresponds to a more intensely stained border in H&E and trichrome staining (Figure 1K-R),  
120 surrounding a mass of less electron-dense necrotic material (Figure 1G-J). Hence, we were able  
121 to establish a correlation between pathophysiological features and changes in electron density.  
122 Additionally, in one lesion (Figure 1G),  $\mu\text{CT}$  revealed two internal “lobe-like” lesions that are not  
123 apparent in the corresponding histopathology (Figure 1K, O), further emphasizing the potential of  
124  $\mu\text{CT}$  to identify unusual pathological features.

125 Overall, these data demonstrate that  $\mu\text{CT}$  can effectively complement standard  
126 histopathological analysis by revealing hidden pathological features that might otherwise be  
127 disregarded by pathologists.

128

### 129 **3D segmentation and spatial distribution of TB lesions in the human lung**

130 While conventional histopathological analysis provides detailed information on very small areas of  
131 interest, it cannot contextualize TB lesions within the overall lung architecture. This has limited our  
132 understanding of the distribution and shapes of lesions within the human TB lung.  $\mu\text{CT}$  has the  
133 potential to improve our understanding of the evolution of granuloma formation and structure,  
134 relative to the diffusion of drugs,  $\text{O}_2$  and nutrients. To contextualize TB lesions relative to the  
135 vasculature and airways, we used  $\mu\text{CT}$  to scan a large slice (~14 x 1.5 x 6 cm) of infected lung at  
136 52.0  $\mu\text{m}$  resolution (Figure 2A, Figure S1, Video S1). 3D segmentation shows that larger lesions  
137 are oriented with a directionality similar to the vasculature and bronchial networks (Figure 2B).

138 Notably, as is evident by the multiple lesions that were curtailed during sectioning of the tissue  
139 ([Figure 2B, lower image](#)), the data suggest that the lesions are more complex as they continue  
140 beyond the sectioning plane. Additionally, airways are absent in areas where lesions predominate,  
141 suggesting that lesion inception through bronchial obstruction has replaced the former airways.

142 Surface area rendering of a sub-section of this sample distinctly identified lesions, blood  
143 vessels and airways ([Figure 2C](#)). 3D segmentation revealed six lesions ([Figure 2D](#)) with volumes  
144 of 23.89, 6.30, 4.09, 4.00, 0.56, and 0.49 mm<sup>3</sup> (total: 39.33 mm<sup>3</sup>, 6.9 % of total tissue volume).  
145 Intense staining of erythrocytes permitted a rapid, albeit partial reconstruction of the vasculature  
146 ([Figure 2E](#)). Vascular destruction, also observed in [Figure 2B](#), contributes to interstitial  
147 hemorrhage resulting in nutrient and O<sub>2</sub> deprivation which further contribute to TB disease. A  
148 considerable degree of hemorrhage was observed with segmentation by thresholding, generating  
149 large complex regions of interest obscuring the lesions and airways ([Figure 2E](#)). There was little, if  
150 any, healthy functional lung tissue within this sample. Lastly, we measured distances between  
151 intact vasculature and necrotic lesions. This proximity would almost certainly impact lesion  
152 development and morphology. The maximum O<sub>2</sub> diffusion distance is 100-200 μm from a blood  
153 vessel<sup>25-27</sup>, and metabolic zonation may account for spatial lesion heterogeneities<sup>28</sup>. Although  
154 histopathological analyses have shown that TB lesion distance from the vasculature can exceed  
155 200 μm, this is not conclusive and could be influenced by the sectioning plane. Using 3D  
156 segmentation, we observed that geometrically, the vasculature follows the curvature of the lesions.  
157 The distances between blood vessels and lesions range from ~0.5 - 1.4 mm ([Figures 2F, S2, S3A,](#)  
158 [S3B](#)). Hence, the curvature of lesions must be considered in order to accurately measure these  
159 distances, which are a crucial factor in understanding how the vasculature delivers nutrients, drugs  
160 and O<sub>2</sub> to bacilli ([Figure S3B](#)) and immune cells in and around the lesion.

161 Our results show that integration of conventional 2D histopathological methods with μCT  
162 provides the means to identify key pathological features such as lesion volume, 3D structure, and  
163 intralesional features in the context of the whole lung. The spatial organization of lesions proximal  
164 to the pulmonary vasculature is particularly important, since vascular destruction will reduce  
165 delivery of anti-TB drugs, O<sub>2</sub> and nutrients. The lack of airways and the directionality of lesions  
166 that accords with the vasculature suggest that TB lesions observed by conventional histopathology

167 may sometimes be cross-sections of obstructed airways instead of spherical lesions. Hence,  
168 application of  $\mu$ CT has substantial potential to advance our understanding of the  
169 pathophysiological mechanisms of TB disease and poor response to anti-TB drugs.

170

171 **Complex 3D structures of TB lesions and communication with the airways**

172 Here, we characterized the spectrum of caseous lesion structures ([Figure 3A](#)) obtained from the  
173 sample in [Figure 2A, B](#) in more detail. In contrast to the current dogma that TB lesions are near-  
174 spherical or ovoid, segmentation of caseous necrotic lesions revealed remarkable morphological  
175 heterogeneity and complexity ([Figure 2A](#)). Of the 40 lesions segmented in [Figure 2A, B](#), multiple  
176 highly branched structures were observed, in contrast to the expected ovoid form. The radius (of  
177 the smallest enclosing sphere) of these lesions ranged from 0.5-7 mm for the more elaborate  
178 forms. While smaller lesions were more spherical, larger lesions were branched with lower  
179 sphericity, which ranged from 0.23-0.6 for all lesions (1.0 is a perfect sphere) ([Figure 3B](#)).

180 Smaller lung samples with caseous necrosis were excised and scanned at higher  
181 resolution, further revealing the complexity of the lesion microenvironment ([Figure 3C-K, Video](#)  
182 [S2](#)). One section taken from the tip of the sample in [Figure 2A, B](#) contained a complex ginger  
183 root-like structure ([Figures 3C-F, Video S3](#)). The sample in [Video S3](#) and a second sample from  
184 a different patient revealed small lobular regions resembling the buds of the "tree-in-bud"  
185 signature often seen in HRCT scans<sup>29,30</sup> of severe TB ([Figures 3H, I, Video S4](#)). We observed  
186 severe hemorrhage as is indicated by the white contrast areas in [Figures 3C, G and J](#) and  
187 vascular destruction in [Figure 3H](#), as well as intricate vasculature that surrounds lesions in both  
188 samples ([Figures 3D, E, H](#)). Both the structures in [Figures 3C-F and G-I](#) continue beyond the  
189 scanned view, indicating that the native, uncut lesions were larger and likely more complex.

190 To further explore the connection between bronchi and TB lesions, i.e., obstructed  
191 airways, we segmented the volumes surrounding lesions, airways and vasculature shown in  
192 [Figure 2A, B](#).  $\mu$ CT reveals darker regions of similar radio-opacity surrounding the necrotic  
193 lesions, airways and blood vessels ([Figure 3J](#)). Segmentation of this volume (indicated in cyan)  
194 reveals that it surrounds and connects granulomas with airways and blood vessels ([Figure 3K](#)).  
195 This further suggests that the shape of TB lesions is dictated by the small airways ([Video S5](#)).

196 Overall, we demonstrate that TB granulomas are remarkably structurally diverse and have  
197 multifaceted connections with the surrounding vasculature and airways. Although 2D  
198 histopathology sectioning typically reveals “round” granulomas that are intuitively inferred to be  
199 spherical, our findings challenge this prevailing dogma. Rather, our results point to a more  
200 complex, cylindrical or branched-type morphology for advanced TB lesions, which are connected  
201 and shaped by the small airways.

202

203 **TB lesion formation through bronchial obstruction**

204 Our  $\mu$ CT data suggest that TB granuloma structure is influenced by the small airways. Here, we  
205 confirm this finding by examining immune cell infiltration and subsequent blockage of small  
206 airways using immunohistochemistry (IHC). Firstly, we confirmed that *Mtb* bacilli were present  
207 intracellularly in macrophages and neutrophils (Figures S4, S5), extracellularly within alveoli  
208 (Figures S4, S5) and within an obstructed bronchus (Figure S6). Next, in highly consolidated  
209 areas of the tuberculous lung (Figure 4A, B and Figure S7), we identified patterns of epithelial cell  
210 remnants consistent with obstructed small airways, as indicated by cytokeratin 7 (CK7), and 3-  
211 mercaptopyruvate sulfur-transferase (3MPST) staining, which is specific for epithelial cells<sup>31</sup>  
212 (Figure 4C-F). This finding demonstrates that immune cell recruitment during TB inflammation can  
213 obstruct the small airways, which can further develop into a granuloma surrounded by epithelial  
214 cells (Figure S8). In less consolidated areas, macrophages, neutrophils and lymphocytes obstruct  
215 alveoli (Figure 4G) leading to independent and coalesced granulomas (Figure 4H), indicative of  
216 the early stages of alveolar consolidation.

217 Next, we examined the contribution of innate and adaptive immune cells to bronchial and  
218 alveolar obstruction. Histopathological appraisal of lung tissue specimens from several TB  
219 patients identified numerous obstructed bronchi containing immune cells (Figure 4I-L). We  
220 identified an abundance of myeloid cell populations, indicated by strong positive staining of  
221 leukocyte common antigen (LCA), myeloid peroxidase (MPO), and CD68 in these cells (Figure  
222 4M, N, O; see Figure S7 for higher power image). Positive staining of CD4+ and CD8+  
223 lymphocytes inside and outside the obstructed bronchus (Figure 4P, Q), and CD20+ cells (Figure  
224 4R) that dominate the area around the bronchus, was observed. Notably, in the consolidated

225     diseased areas in [Figure 4M-R](#) (boxes), we observed clear evidence of myeloid cell and lymphoid  
226     cell infiltration by IHC ([Figure S9A-F](#)), which is in support of the consolidation shown in [Figure 4A-F](#).  
227     Lastly, we observed necrotic material and immune cells from TB granulomas spilling into a  
228     bronchus ([Figure 4S-U](#); see [Figure S10](#) for high power image), providing compelling evidence for  
229     expansion of necrotic lesions along the airway network to help shape granuloma structure. These  
230     granulomas are surrounded by foam cells ([Figure S11](#)), consistent with historical studies showing  
231     that obstructive lobular pneumonia softens lung tissue (i.e., caseating necrosis), which is then  
232     coughed up, leading to cavitation<sup>13,32</sup>.

233           In conclusion, histopathology and IHC data are fully consistent with our  $\mu$ /nCT data  
234     demonstrating that recruitment and expansion of immune cells in the airways, eventually followed  
235     by necrosis, contribute to blockage of the airways and the 3D shape of the granuloma. These  
236     findings have implications for how TB transmission is triggered through coughing, for cavity  
237     formation, and for aerosolized drug delivery strategies.

238

## 239     **Discussion**

240     While conventional histological methods have been the gold standard for appraising TB disease  
241     pathology for over 100 years, there is a need to address the multidimensionality of diseased tissue  
242     using advanced high-resolution imaging modalities. Our current understanding of TB disease has  
243     been shaped by the histopathological interpretations in the 1940s and 1950s by Arnold R. Rich<sup>1</sup>,  
244     George Canetti<sup>2</sup> and Edgar M. Medlar<sup>33,34</sup> when post-mortem and resected human lung tissues  
245     were routinely available. With the emergence of HIV and its synergism with TB, and broad access  
246     to anti-TB drugs, all of which influence disease pathology<sup>35-37</sup>, it is reasonable to suppose that TB  
247     pathology phenotypes have changed. Difficulty in describing human pulmonary TB disease has  
248     hampered the TB field for decades, whereas the use of animal models for TB has flourished.  
249     Unfortunately, no single animal model accurately duplicates the full spectrum of human pulmonary  
250     TB phenotypes. Here,  $\mu$ CT imaging has provided new insight into the morphologies of human  
251     necrotic TB lesions, demonstrating that they can form branched and cylindrical structures with  
252     large variations in volume, size and spatial distribution and that they are connected to the small

253 airways. These findings contrast with the current dogma that granulomas are spherical, an  
254 understandable conclusion based on conventional histopathology. Our findings exemplify how 3D  
255 visualization of TB disease pathophysiology can improve our understanding of the evolution of TB  
256 granuloma and provide a foundation for a 3D atlas of the human tuberculous lung. Lastly, our  
257 findings establish a clinically relevant framework for the discovery of imaging biomarkers as  
258 diagnostic indicators, and provide a strong rationale for development of aerosolized anti-TB drug  
259 delivery strategies.

260 A significant advance in this study is the application of 3D segmentation to the  
261 microarchitecture of the tuberculous lung, which provides detailed insight into the spatial  
262 relationship between TB granulomas, airways, and the vascular system. To our knowledge, such  
263 findings have not yet been reported for any pulmonary pathogen, bacterial or viral. Several  
264 unexpected discoveries about the TB granuloma were made. Firstly, demonstrating that the TB  
265 granuloma represents a spectrum of complex, branched-type morphologies, and is shaped by the  
266 small airways, has implications for understanding the evolution of granuloma, of which little is  
267 known. This new insight represents an important advance with strong clinical implications since  
268 the prevailing presumption has been that the granuloma is spherical<sup>3-11</sup>. Also, our 3D  
269 segmentation highlights the possibility that a single structurally complex lesion could be  
270 erroneously viewed as multiple independent lesions when evaluated in 2D. The potential for  
271 misinterpretation of granuloma number, size or position indicates that great care must be taken  
272 while interpreting "-omic" data derived directly from TB lesions, as conclusions will be influenced  
273 by the actual (but unknown) 3D shape of the lesion. Further, conclusions drawn regarding  
274 microenvironments surrounding what appear to be multiple granulomas could change if it were  
275 understood that a single complex lesion was under investigation. Secondly, our findings highlight  
276 the pathophysiological factors that help dictate the shape of the granuloma. Here, it is evident that  
277 immune cell infiltration in the alveoli, bronchioles and bronchi dictate the shape, and that immune  
278 cell recruitment and subsequent necrosis expand in the airways to follow "the path of least  
279 resistance". Alveolar walls contain numerous inter-alveolar pores that may function as conduits for  
280 the dissemination of *Mtb* or infected cells. Also, several granulomas in this study are reminiscent  
281 of the tree-in-bud form, an HRCT signature that is present in virtually all cases of active pulmonary

282 TB<sup>29,30</sup>. Thirdly, the spatial relationship between TB lesions and pruning of the surrounding  
283 vasculature, which impedes the delivery of nutrients, O<sub>2</sub>, anti-TB drugs and immune cells to  
284 granulomas, may shed light on the complex pathophysiology involved in promoting persistence  
285 and drug tolerance. For example, 3D renderings of the vascular system from diseased TB lungs  
286 show destruction of the vascular network, which would reduce delivery of anti-TB drugs,  
287 metabolites, and O<sub>2</sub>. This may explain why drugs do not reach bactericidal concentrations within  
288 TB lesions<sup>38</sup> and how *Mtb*, which requires O<sub>2</sub> to grow, is able to persist long-term in O<sub>2</sub>-deficient  
289 lesions, presumably in a state of metabolic shutdown. For instance, the maximum O<sub>2</sub> diffusion  
290 distance is ~200 μm<sup>25-27</sup> after which tissue becomes hypoxic. By accurately measuring the  
291 distance between blood vessels and the segmented TB lesions, we conclude that many necrotic  
292 lesions are hypoxic. Based on a recent study<sup>28</sup>, it is almost certain that gradients, or zones, of  
293 drugs, metabolites and O<sub>2</sub> exist within TB lung tissue. Therefore, separate anisotropic gradients  
294 for different drugs<sup>38,39</sup> may trigger sequential development of *Mtb* drug resistance or tolerance by  
295 passaging through environments with low drug concentrations. Therefore, therapeutic  
296 angiogenesis and aerosolized drug delivery strategies<sup>40</sup> may represent plausible approaches to  
297 increase anti-TB drug levels in the granuloma.

298 Our findings also suggest our approach is transformative for histopathological assessment  
299 as it will contribute to a more informative clinicopathological analysis for TB. Notably, all our  
300 histological sections could be matched to the corresponding sliced plane from the μCT 3D volume.  
301 Consistent with autopsy studies<sup>20</sup>, these findings provide further insight into the evolution of TB  
302 lesions, and suggest that necrotic material fills the bronchiolar lumen to induce bronchial wall  
303 necrosis, which promotes progressive necrosis of the lesion. Furthermore, integration of μCT  
304 imaging with histopathology has strong potential to influence other disciplines including pathology,  
305 biomedical imaging, infectious diseases and cancer, ultimately leading to new discoveries.  
306 Overall, our data demonstrate that μ/nCT is a powerful imaging tool to study the mechanism of  
307 granuloma formation.

308 Our study has some limitations. First, this was a focused study and a limited number of  
309 lung tissue samples were examined from TB patients with diverse medical histories and  
310 treatments; hence it is likely that a larger test cohort may render a more representative disease

311 spectrum. However, sampling from different regions of each lung allowed us to evaluate  
312 microenvironments at different stages of tissue pathology. Second, we used iodine, a widely  
313 employed contrast agent, in our studies; however, other agents may provide unique staining  
314 patterns that allow identification of different adjacent tissues. This is especially true if reversible  
315 staining protocols can be developed that allow serial staining with different contrast agents.  
316 Contrast staining with iodine also interfered with subsequent hematoxylin staining for histological  
317 follow-up and requires further optimization. Lastly, similar to conventional histopathology,  
318 shrinkage of tissue during formalin fixation and staining is widely known and may influence volume  
319 calculations. However, this could be mitigated by use of polyoxometalates<sup>41</sup>.

320 Overall, our findings have important implications for TB disease treatment and diagnosis as  
321 several surprising findings were made, including the spectrum of granuloma 3D structures, the  
322 size and volume of TB lesions, and their spatial organization in relation to the vasculature and  
323 airways. Secondly, scouting for pathological features may help guide and expedite  
324 histopathological follow-up studies. Thirdly, digitized 3D image libraries of tissue and organs from  
325 TB patients could be used to identify novel imaging biomarkers based on patterns of differential  
326 radio-opacities<sup>42</sup> and establishment of a 3D reference atlas of the tuberculous lung. Lastly, our  
327 findings suggest that aerosolized anti-TB drug delivery strategies for the control of TB should be  
328 reconsidered.

329

330 **Methods**

331

332 **Ethics and Human Subjects**

333 This study was approved by the University of KwaZulu-Natal Biomedical Research Ethics  
334 Committee (Class approval study number BCA 535/16). Patients undergoing lung resection for TB  
335 (Study ID: BE 019/13) were recruited from King Dinuzulu Hospital Complex, a tertiary center for  
336 TB patients in Durban, South Africa. *Mtb*-infected human lung tissues are routinely obtained  
337 following surgery for removal of irreversibly damaged lobes or lungs (bronchiectasis and/or  
338 cavitary lung disease). Written informed consent was obtained from all participants. All patients  
339 undergoing lung resection for TB had completed a full 6-9-month course of anti-TB treatment, or  
340 up to 2 years of treatment for drug-resistant TB. Patients were assessed for extent of pulmonary  
341 disease (cavitation and or bronchiectasis) via HRCT. The fitness of each patient to withstand a  
342 thoracotomy and lung resection was determined by Karnofsky score, six-minute walk test,  
343 spirometry and arterial blood gas. Assessment of patients with massive hemoptysis included their  
344 general condition, effort tolerance prior to hemoptysis, arterial blood gas measurement, serum  
345 albumin level and HRCT imaging of the chest. On gross assessment, all pneumonectomies or  
346 lobectomies were bronchiectatic, hemorrhagic, variably fibrotic and atelectatic and contained  
347 visible tubercles (Table 1).

348

349 **Sample Preparation**

350 Seven tissue samples (Samples A – G, Table 2) from resected human lungs (un-inflated) ([Table 1](#))  
351 were selected for  $\mu$ /nCT analyses. All samples were fixed in 10% buffered formalin for at least 14  
352 days. Samples A and B were obtained from resected lungs with evidence of cavitation and  
353 *Aspergillus* infection in sample B. Samples C and D represent relatively healthy tissue from a  
354 cancerous lung and *Mtb*-infected lung, respectively. Sample E was selected from a lung with  
355 evidence of severe TB infection including extensive caseous necrosis. Samples F and G exhibit  
356 calcification, as well as fungal infection in F. Samples B-E were contrast stained with iodine by

357 immersing the samples in 2.5 % Lugol's solution for 1-5 days depending on the size of the sample.  
358 Samples F and G were also mounted in paraffin wax blocks before scanning.

359 For  $\mu$ /n-CT scanning, samples were mounted on or in 50 ml falcon tubes using a  
360 combination of cellophane tape and florist foam. Non-paraffin embedded samples were lodged  
361 above ~ 5 ml formalin in the bottom of the tube with polystyrene foam and lodged between the  
362 walls of the tube to prevent shifting of the sample. The low density of polystyrene foam also  
363 enables easy deletion from the reconstructed volume during subsequent visualization and  
364 analysis. The tube was then sealed with parafilm for the duration of the scan to maintain a moist  
365 atmosphere and prevent desiccation. Prior to mounting, samples were rinsed with water and  
366 dabbed dry to remove excess staining solution.

367

### 368 **$\mu$ /nCT scanning**

369 A General Electric Phoenix V|TomeX L240 system was used for  $\mu$ CT (2024x2024 pixel image, 16  
370 bit depth) was used for  $\mu$ CT with a resolution range of 12.0 – 60.0  $\mu$ m. A General Electric Phoenix  
371 Nanotom S (2304x2304 pixel image, 16 bit depth) was used for nCT with a resolution (isotropic  
372 voxel size) range of 4.1 - 16.0  $\mu$ m. Although the instrument is capable of sub- $\mu$ m resolution for  
373 small samples, none of the samples analyzed in this study were small enough. All samples were  
374 scanned over 360°. A range of settings were used to scan the samples as described further in  
375 Table 1. Briefly, voltage varied between 50-160 kV, current varied between 200-1000  $\mu$ A and  
376 scanning times ranged from 2000-5400 seconds. For most scans a tungsten target was  
377 employed. A molybdenum target was used for two n-CT scans (Table 2).

378

### 379 **Image Processing and volume rendering**

380 Volumes were reconstructed with system-supplied General Electric Datos software. Subsequent  
381 visualization and analysis (such as volume and density calculations) were performed in Volume  
382 Graphics VGStudio Max 3.1 or 3.2. Where possible, simple thresholding was employed for  
383 segmentation (demarcation of 3D regions of interest), followed by semi-automated segmentation  
384 using the VGStudio Max region growing tool. The region growing tool allows for manual selection  
385 of a 3D scan region based on adjustable intensity thresholds and different intensity averaging

386 schemes. Two approaches were used for segmenting vasculature with the region growing tool.  
387 Firstly, by using a stringent threshold and selecting a voxel near the center of a brightly stained  
388 vessel it is possible to rapidly generate branched segmentations that do not overlap into non-  
389 vascular tissue. Secondly, individual vessels can be manually extended by selecting adjacent  
390 volumes within an overlapping sphere and careful adjustment of the thresholds for intensity values  
391 with smaller differences to non-vascular tissue. This latter mode was also used for segmenting  
392 necrotic lesions. For complex heterogeneous datasets this is needed to segment intricate  
393 structures without including adjacent voxels that represent a different tissue. To correlate with  
394 histopathology, the axes of the 3D volume were adjusted (re-registered in VGStudio Max parlance)  
395 followed by slicing through the volume to match the 2D histology image as closely as possible with  
396 three or more diseased and healthy parenchymal features (airways, blood vessels, lesions, etc.)  
397

### 398 **Histopathology**

399 Identification of anatomical features and pathology in the CT scans was confirmed by histological  
400 techniques using Hematoxylin and Eosin (H&E) or Masson's trichrome stain. Briefly, samples of  
401 lung were aseptically removed and fixed in 10% buffered formalin and processed in a vacuum  
402 filtration processor using a xylene-free method with isopropanol as the main substitute fixative.  
403 Tissue sections were embedded in paraffin wax. Sections were cut at 4  $\mu$ m, baked at 60°C for 15  
404 min, dewaxed through two changes of xylene and rehydrated through descending grades of  
405 alcohol to water. These sections were stained with H&E or the Masson's trichrome method using  
406 standard procedures. Slides were dehydrated in ascending grades of alcohol, cleared in xylene,  
407 and mounted with a mixture of distyrene, plasticizer, and xylene.  
408

### 409 **Histology slide digitization and cross validation with $\mu$ /n-CT imaging**

410 Human lung specimens were digitized using a Hamamatsu NDP slide scanner (Hamamatsu  
411 NanoZoomer RS2, Model C10730-12) and its viewing software (NDP.View2). The red, green, and  
412 blue color balance was kept at 100% whereas gamma correction was maintained between 0.7 and  
413 2. Brightness (60–110%) and contrast (100–180%) settings vary slightly between slides  
414 depending on staining quality. Resolution was ~230 nm/pixel yielding a file size of ~2-4.4 GB.

415 Contrast, brightness and intensity of exported images (jpg format) were minimally adjusted using  
416 CorelDraw X8. Registration of the  $\mu$ /nCT scans against histopathology images was performed  
417 manually in VGStudio Max by using blood vessels, bronchi and lesions as landmarks.

418

419 **Immunohistochemistry**

420 Pulmonary tissue was cut into 2-4  $\mu$ m thick sections, mounted on charged slides, and heated at  
421 56° C for 15 min. Sections were dewaxed in xylene followed by rinse in 100% ethanol and one  
422 change of SVR (95%). Slides were then washed under running water for two min followed by  
423 antigen retrieval via Heat Induced Epitope Retrieval (HIER) in Tris-sodium chloride (pH 6.0) for 30  
424 min. Slides were cooled for 15 min and rinsed under running water for two min. Endogenous  
425 peroxide activity was blocked using 3 % hydrogen peroxide for 10 min at room temperature (RT).  
426 Slides were then washed in PBST and blocked with protein block (Novolink) for 5 min at RT.  
427 Sections were incubated with primary antibodies for cytokeratin 7 (CK7; OV-TL  
428 12/30, DAKO, Ready-to-Use), 3-mercaptopyruvate sulfurtransferase (MPST; NBP1-82617, Novus  
429 Biologicals, 1:100), CD68 (M0814-CD68-KP1, DAKO, 1:3000), LCA (M0701-CD45-2B11+PD7/26,  
430 DAKO, 1:200), MPO heavy chain (sc-34161, SantaCruz Biotechnology, 1:100), CD4 (NCL-CD4-  
431 1F6, Novocastra, 1:50), CD8 (NCL-L-CD8-295-1A5, Novacastra, 1:80), CD20 (M0755-CD20cy-  
432 L26, DAKO, 1:1000), acid sphingomyelinase (ASM; ab83354, ABCAM, 1:1000) followed by  
433 washing and incubation with either HRP anti-rabbit IgG HRP (ab6721, abcam), or the polymer  
434 (Novolink) for 30 min at RT. Slides were then washed and stained with DAB for 5 min, washed  
435 under running water and counterstained with hematoxylin for 2 min. Slides were rinsed under  
436 running water, blued in 3% ammoniated water for 30 s, washed under water, dehydrated and  
437 mounted in Distyrene Plasticiser Xylene (DPX). For isotype control sections, a similar protocol to  
438 our previous studies was followed<sup>24,31</sup>; either IgG4 (LS-C70325/27332) or rabbit IgG (ab37415,  
439 Abcam) was used (at the same concentration/dilution as the primary antibodies) in place of the  
440 primary antibodies (isotype control).

441

442

443

444 **IHC/Ziehl Neelsen (ZN) combination staining**

445 The IHC protocol was followed as described above, but the hematoxylin counterstain step was  
446 eliminated, and the ZN histochemical staining was continued. Slides were incubated with heated  
447 Carbol-Fuchsin stain for 10 min and then washed under running tap water. 3% acid alcohol was  
448 applied to the slide to decolorize for 30 s or until sections appeared clear. Slides were then  
449 washed in running tap water for 2 min. Slides were then counter stained with methylene blue,  
450 rinsed under running water, dehydrated and mounted using DPX mounting media.

451

452 **Numerical analysis and plotting**

453 Opacity plots, histograms and scatterplots were generated using Python 3.7 in the Jupyter  
454 notebook environment with the Matplotlib, Seaborn and Pandas libraries.

455

456 **Data availability**

457 High resolution histopathology and  $\mu$ /n-CT images or videos will be provided upon request or can  
458 be downloaded at: <https://www.ahri.org/scientist/adrie-steyn/>. Please contact Dr. Adrie J.C. Steyn  
459 ([adrie.steyn@ahri.org](mailto:adrie.steyn@ahri.org) or [asteyn@uab.edu](mailto:asteyn@uab.edu))

460

461 **Acknowledgements** This work was supported by NIH grants R01AI111940, R01AI134810,  
462 R01AI137043, R61/33AI138280, R21A127182, a Bill and Melinda Gates Foundation Award  
463 (OPP1130017) (AJCS) and pilot funds from the UAB CFAR, CFRB and Infectious Diseases and  
464 Global Health and Vaccines Initiative to AJCS. The research was also co-funded by CRDF  
465 Global, the South African Medical Research Council, and an NRF BRICS Multilateral grant to  
466 AJCS.

467

468 **Author contributions** Conceptualization and Design: GW, AJCS. Lung tissue preparation: GW,  
469 KN, KL.  $\mu$ /nCT scanning, AP, SA. HRCT: RM, KM, LYP, MM. Pathology: PKR, TN,  
470 Histopathology: KN, KL, RLH. 3D segmentation: GW, AD, LC. Data integration: GW, JNG, AJCS.  
471 Writing initial draft: GW, JNG, AJCS. Editing: JNG, AJCS. Final draft: All authors. Figure  
472 preparation: GW, AJCS. All authors discussed the results and commented on the manuscript.

473

474 **Competing interests.** The authors declare no competing interests.

475

476 **Table 1. Clinical characteristics of human subjects.**

#	Patient #	Age	Sex	Type	Macroscopic and Microscopic features	Type of resection
1	202134	38	F	TB	Caseative necrosis, 2 cm cavity in upper lobe, identifiable acid-fast bacilli, suppurative granulomas with microabscess formation	Left pneumonectomy
2	202203	67	M	TB	Necrotizing granulomatous inflammation with acid-fast bacilli, intra-alveolar foamy macrophages are present	Left upper lobe lobectomy,
3	202211	32	F	TB	Cavitation and miliary TB, fibrocalcific nodules, acid-fast bacilli present within macrophages, features of lymphoid interstitial pneumonia are present	Left pneumonectomy
4	202294	39	F	TB	Necrotizing granulomatous inflammation and hemorrhage, granulomas with central microabscesses are present, acid-fast bacilli stain is positive	Left upper lobe lobectomy
5	202254	37	F	TB	Caseous necrosis with cavity containing necrotic material, necrotizing granulomatous inflammation, Langhan's giant cells are present, paucibacillary	Right lower lobe lobectomy
6	202733	37	F	TB	Multiple round tubercles were noted, necrotizing and non-necrotizing granulomatous inflammation, acid-fast bacilli positive, Langhans giant cells are present, alveolar spaces filled with eosinophilic material and hemorrhage	Right upper lobe lobectomy
7	202194	15	F	TB	Multiple tubercles confirm active necrotizing granulomas, acid-fast bacilli were seen, vasculitis, interstitial fibrosis	Right upper lobe lobectomy
8	202172	28	M	TB	Shrunken, collapsed tubercles appear irregular in shape, calcified foci were confirmed, focal tuberculous scars and fibrocaseous foci were noted, intra-alveolar siderophages, paucibacillary	Left upper lobe lobectomy
9	202156	33	F	TB	Shrunken lung, collapsed with bronchiectasis and fibrosis, tubercles irregular in shape, irregular cavity was noted, granulation tissue is prominent, aspergillosis, paucibacillary	Left pneumonectomy
10	202187	45	F	XDR TB	Necrotizing granulomatous inflammation, granulomas surrounding central areas of caseous necrosis, Langhan's giant cells are present, cavities contained neutrophils, acid-fast bacilli are present	Right pneumonectomy
11	202510	50	M	TB	Bronchiectatic, contains cavity wall lined by chronic suppurative inflammation, granulation tissue and foamy histiocytes were observed, aspergilloma was present, hemorrhage, or oedema and organizing pneumonia were seen	Right pneumonectomy
12	202126	37	F	TB	Bronchiectatic cavitation and caseous necrosis, fibrocalcific and fibrocaseous granulomas were noted, histiocytes, giant cells and central areas of necrosis predominate, intra-alveolar foamy histiocytes, paucibacillary	Right pneumonectomy
13	202340	65	F	TB	Irregular tubercles with bronchopneumonia were identified, extensive granulomatous inflammation, acid-fast bacilli were identified, interstitial fibrosis and areas of gross scarring	Right pneumonectomy
14	202113	24	M	TB	Necrotizing granulomatous inflammation with acid-fast bacilli, some of the granulomas contained suppurative centres, acid-fast bacilli were identified, granulomatous process is also seen within the hilar lymph nodes	Left upper lobe lobectomy
15	202221h				Healthy lung control	
16	202254h				Healthy lung control	
17	202223h				Healthy lung control	

**Table 2. Scanning settings.** All  $\mu$ CT scans were performed at 16-bit depth

Figures	Sample	Target	Instrument	Scan time (s)	Averaging	Skip	Resolution ( $\mu$ m)	Voltage (kV)	Current ( $\mu$ A)	Images	Preparation
Figure 1B, E-J Figure 2C-F Figure 3J, K. Figure S9 Video S5	A	W	$\mu$ CT	3000	5	1	12.0	160	200	3000	Contrast stained with $I_2$
Figure 6A Video S1	B	W	$\mu$ CT	3000	5	1	52.0	160	260	3000	Contrast stained with $I_2$
Figure 2A-F Video S2, S3	C	W	$\mu$ CT	2700	5	1	15.0	160	180	2700	
Figure 2G-I Figure S8 Video S4	D	W	$\mu$ CT	2800	5	1	15.0	80	400	2800	Contrast stained with $I_2$

## Figures Legends

### Figure 1. $\mu$ CT and histology of human TB-lung with caseous necrosis (Sample A)

(A) Gross image of sample E exhibiting caseous necrosis. Pink circles indicate blood vessels. (B)  $\mu$ CT (12.0  $\mu$ m resolution) of sample E, caseous necrosis (yellow, "L"), hemorrhage/blood (red). (C) H&E histology of (B) (D) MT histology of (B). (E-J) Necrotic regions have a 'halo-like' appearance, with a slightly brighter outer shell (green arrows) surrounding a slightly darker interior (yellow arrows). Necrotic regions are surrounded by a dark border (blue arrows). (E, F) Typical X-ray opacity profile/electron density (yellow graph) across necrotic lesions measured along the green axis. Dark fibrotic regions are followed by a slightly opaquer ring that surrounds the (lighter) lesion. (G-J) Representative  $\mu$ CT images of caseous necrotic lesions. (K-N) H&E and (O-R) MT histology corresponding to panels G-J reveal the darker shell (blue arrows) surrounding the necrotic regions that corresponds to fibrotic tissue.

### Figure 2. $\mu$ CT and segmentation of human TB-lung with caseous necrosis (Sample B)

(A) 2D slice of  $\mu$ CT (52.0  $\mu$ m resolution) of a human lung lobe. Necrotic lesions (yellow), bronchi/bronchioles (blue) and vasculature (red) are outlined. (B) Complex necrotic lesions are oriented similarly to the airways and vasculature. 3D renderings of lesions (yellow), bronchi/bronchioles (blue) and vasculature (red) segmentation. Lower image: side view of A with truncated lesions (also observed in D) indicated by vertical arrows. (C) Sample B exhibiting caseous necrosis. ScatterHQ (VGL Studio) rendering of surface electron density. L, truncated lesion; Br, bronchiole/airway; Bv, blood vessel. (D) 3D segmentation of blood vessels (red, Bv), airways (blue, Br) and necrotic lesions (yellow, L). (E) 3D segmentation of lesions (yellow) and hemorrhage (red/orange). Blood vessels and nearby regions of bleeding stain brightly, with decreasing intensity further away from blood vessels. By selecting all regions above a high intensity threshold (red, H2), hemorrhaging (including

intact vasculature) can be quickly segmented. The lower threshold (orange, H1) also selects other components outside hemorrhaged region (e.g, within the lesions). (F) Representative  $\mu$ CT slice of segmented regions from (D) demonstrating the distance between the lesions and the vasculature.

**Figure 3. Lesion morphological heterogeneity and micro-structure of lesions and surrounding vasculature (Samples A-D).**

(A) The morphology of necrotic lesions in advanced TB (Sample B) ranges from small nodules (mm scale) to large branched structures (cm scale) within a lung sample. (B) Relationship between lesion size and shape in Sample B. Sphericity is the ratio of the surface area of the sphere with the same lesion volume to the lesion surface area. Smaller lesions tend to be nodular (higher sphericity), while larger lesions exhibit more complex shapes with a lower sphericity. (C-F)  $\mu$ CT of Sample C, obtained from the tip of Sample B. (C) 2D slice of tip of Sample B. (D) 3D rendering of lesion (yellow) and vasculature (red) segmentation in relation to X-ray absorption/electron density. (E) 3D rendering of lesion (yellow) and vasculature (red) segmentation in relation to sample surface. (F) 3D rendering of lesion (yellow) only. (G-I)  $\mu$ CT of Sample D. (G) 2D slice of Sample D. (H) 3D rendering of lesion (yellow) and vasculature (red) segmentation in relation to X-ray absorption/electron density. Yellow arrow; hemorrhage, purple and turquoise structures; obliterated airways. (I) 3D rendering of lesion (yellow) only. Dotted circle: area resembling tree-in-bud. (J) 2D slice of Sample A (excised from Sample B). (K) 3D rendering of lesions (yellow), vasculature (red), bronchus (green) and lesions/vasculature/airway connections (cyan) from (J).

**Figure 4. Histopathology of the small airways of an *Mtb*-infected human lung.**

(A, B) Low power magnification of H&E stain in lung parenchyma. (C, D) Low power and (E, F) medium power magnification of epithelial staining in the adluminal layer (C, E; CK7, D, F; 3MPST). (G, H) Combined CD68 and ZN staining. Circled areas: alveoli filled with macrophages, arrows; giant cells. Yellow arrows; *Mtb*. (I, J, K, L) H&E staining of bronchial

obstruction. (M, N, O, P, Q, R) IHC of myeloid and lymphocytes. Boxed areas; see [Figures S7 and S9](#). (S) Low power magnification of ASM (nuclear) staining. Note the spilling of necrotic material from granulomas (NG) into an airway. (T) Medium power image (black asterisks, cartilage, BEL; bronchial epithelial layer, black arrows; spillage of necrotic material into bronchus, Br; bronchus). (U) High power depiction of the BEL (yellow asterisk) with immune cells in the airway. Red arrows; neutrophils. RBC; red blood cells. See [Figure S10](#) for high-power image.

## Supplemental Figure Legends

**Figure S1. Gross image of lung section scanned using  $\mu$ CT.** (A) Sample E; excised from a lung portion exhibiting several necrotic lesions, fibrosis, bronchiectasis, and calcification.

**Figure S2. Distances between lesions and intact vasculature.** Typical distances between segmented lesions (yellow) and intact vasculature (red). The  $\mu$ CT slice (left) and segmentation (right) are shown.

**Figure S3. Distances between lesions and intact vasculature.** H&E histology (A) showing distances from intact vasculature (inset i and ii) demonstrating evidence of vascular pruning of the TB lesion, strongly suggestive of lesion hypoxia. (B) low power depiction of ZN stain showing the distances between a large aggregate of *Mtb* cells (i), and single *Mtb* cells closest to the vasculature (ii) demonstrating that bacilli are exposed to a hypoxic environment.

**Figure S4. High power depiction of intracellular and extracellular *Mtb* in alveoli.** Combined CD68 IHC and ZN stain. Yellow arrows indicate extracellular or intracellular (neutrophil) *Mtb*.

**Figure S5. High power depiction of intracellular and extracellular *Mtb* in alveoli.** Combined CD68 IHC and ZN stain. Yellow arrows indicate extracellular or intracellular (macrophage) *Mtb*.

**Figure S6. High power depiction of intracellular and extracellular *Mtb* in the luminal and adluminal areas.** Combined CD68 IHC and ZN stain of an obstructed bronchus containing numerous immune cells. Yellow arrows indicate intracellular and extracellular *Mtb*. Inset; high power contrast enhanced image of a large aggregate of likely intracellular *Mtb* cells (box). \*Bronchial epithelial layer.

**Figure S7. Low power image of obstructed bronchus.** Low power image of H&E of obstructed bronchus used in [Figure 4](#) (A, C, E, M, N, O, P, Q, R, S) and [Figure S9](#). BEL; bronchial epithelial layer, L; lumen with immune cells. Box; area examined using IHC ([Figure S9](#)).

**Figure S8. Medium power image of granuloma.** Medium and high-power images of a *Mtb* granuloma stained for epithelial cells using 3MPST Ab.

**Figure S9. IHC of a select area in Figure 4 and Figure S7.** Staining for (A) CD68, (B) MPO, (C) LCA, (D) CD4, (E) CD 8, and (F) CD20 Abs in the consolidated area of [Figure S7](#).

**Figure S10. High power magnification of Figure 4 S-U.**

**Figure S11. H&E stain of area containing foam cells.** Low power (encircled with dotted line) and high power (boxed) images of foam cells scattered around granulomas in [Figure 4 S-U](#) and [Figure S10](#).

## **Video Legends**

**Video S1. Relative orientation and directionality of caseous necrotic lesions, airways and vasculature (Sample B).** Segmentation of caseous lesions within in slice of diseased lung reveals complex morphology, and a similar orientation to remaining airways and vasculature. Where there is a paucity of airways, lesions dominate, suggesting airway obstruction and bronchial spread of infection where the lesion acts as its source.

**Video S2. Slice video of  $\mu$ CT scan of caseous necrosis (Sample C).**  $\mu$ CT scan through Sample M (tip of Sample B). Caseous lesions are outlined in yellow and vasculature in red. Note the cylindrical shape of the lesion. HRCT scans refer to such lesions as tree-in-bud.

**Video S3. Segmentation of caseous necrotic lesion and surrounding vasculature (Sample C, removed from Sample B).** Caseous necrosis is outlined in yellow, vasculature in red. The vasculature “hugs” the surface of the lesions.

**Video S4. Segmentation of caseous necrotic lesion with embedded obliterated structures and surrounding vasculature (Sample D).** Caseous necrosis is shown in yellow, vasculature in red. Obliterated structures within the lesions could also be segmented (purple), revealing a branched structure resembling a former airway.

**Video S5. Segmentation of volumes connecting necrotic lesions with airway and vascular networks (Sample A).** Lesions (yellow), vasculature (red), airways (blue) and surrounding volumes (cyan) were segmented. The surrounding volumes around lesions, airways and vasculature are contiguous. This further demonstrate caseous necrotic lesions form within (or heavily influence) airways and are shaped by transport network morphology.

## References

- 1 Rich, A. R. *The pathogenesis of tuberculosis*. Second Edition edn, (C.C. Thomas, 1944).
- 2 Canetti, G. *The tubercle bacillus in the pulmonary lesion of man: histobacteriology and its bearing on the therapy of pulmonary tuberculosis*. (Springer Publishing Company, 1955).
- 3 Silva Miranda, M., Breiman, A., Allain, S., Deknuydt, F. & Altare, F. The tuberculous granuloma: an unsuccessful host defence mechanism providing a safety shelter for the bacteria? *Clinical & Developmental Immunology* **2012**, 139127, doi:10.1155/2012/139127 (2012).
- 4 Gil, O. *et al.* Granuloma encapsulation is a key factor for containing tuberculosis infection in minipigs. *PLoS One* **5**, e10030, doi:10.1371/journal.pone.0010030 (2010).
- 5 Marino, S., El-Kebir, M. & Kirschner, D. A hybrid multi-compartment model of granuloma formation and T cell priming in tuberculosis. *Journal of Theoretical Biology* **280**, 50-62, doi:10.1016/j.jtbi.2011.03.022 (2011).
- 6 Ordonez, A. A. *et al.* Radioiodinated DPA-713 imaging correlates with bactericidal activity of tuberculosis treatments in mice. *Antimicrob Agents Chemother* **59**, 642-649, doi:10.1128/AAC.04180-14 (2015).
- 7 Prats, C. *et al.* Local Inflammation, Dissemination and Coalescence of Lesions Are Key for the Progression toward Active Tuberculosis: The Bubble Model. *Frontiers in Microbiology* **7**, 33, doi:10.3389/fmicb.2016.00033 (2016).
- 8 Hao, W., Schlesinger, L. S. & Friedman, A. Modeling Granulomas in Response to Infection in the Lung. *PLoS One* **11**, e0148738, doi:10.1371/journal.pone.0148738 (2016).
- 9 Pienaar, E. *et al.* Comparing efficacies of moxifloxacin, levofloxacin and gatifloxacin in tuberculosis granulomas using a multi-scale systems pharmacology approach. *PLoS Computational Biology* **13**, e1005650, doi:10.1371/journal.pcbi.1005650 (2017).
- 10 Goldberg, M. F. *et al.* Salmonella Persist in Activated Macrophages in T Cell-Sparse Granulomas but Are Contained by Surrounding CXCR3 Ligand-Positioned Th1 Cells. *Immunity* **49**, 1090-1102 e1097, doi:10.1016/j.jimmuni.2018.10.009 (2018).
- 11 Lin, P. L. & Flynn, J. L. CD8 T cells and *Mycobacterium tuberculosis* infection. *Seminars in Immunopathology* **37**, 239-249, doi:10.1007/s00281-015-0490-8 (2015).
- 12 Hunter, R. L. Pathology of post primary tuberculosis of the lung: an illustrated critical review. *Tuberculosis* **91**, 497-509, doi:10.1016/j.tube.2011.03.007 (2011).
- 13 Hunter, R. L. Tuberculosis as a three-act play: A new paradigm for the pathogenesis of pulmonary tuberculosis. *Tuberculosis* **97**, 8-17, doi:10.1016/j.tube.2015.11.010 (2016).
- 14 Yeh, J. J. *et al.* High-resolution CT for identify patients with smear-positive, active pulmonary tuberculosis. *Eur J Radiol* **81**, 195-201, doi:10.1016/j.ejrad.2010.09.040 (2012).
- 15 Marchiori, E., Zanetti, G., Barreto, M. M., de Andrade, F. T. & Rodrigues, R. S. Atypical distribution of small nodules on high resolution CT studies: patterns and differentials. *Respir Med* **105**, 1263-1267, doi:10.1016/j.rmed.2011.02.010 (2011).
- 16 Lee, S. W. *et al.* The role of chest CT scanning in TB outbreak investigation. *Chest* **137**, 1057-1064, doi:10.1378/chest.09-1513 (2010).
- 17 Kampschulte, M. *et al.* Nano-Computed Tomography: Technique and Applications. *RöFo - Fortschritte auf dem Gebiet der Röntgenstrahlen und der bildgebenden Verfahren* **188**, 146-154, doi:10.1055/s-0041-106541 (2016).
- 18 Bajaj, S. K. & Tombach, B. Respiratory infections in immunocompromised patients: Lung findings using chest computed tomography. *Radiology of Infectious Diseases* **4**, 29-37, doi:10.1016/j.rjid.2016.11.001 (2017).

19 Nakamoto, K. *et al.* Multi-drug-resistant tuberculosis with galaxy and cluster signs on high-resolution computed tomography: MDR-TB with galaxy and cluster signs. *Respirology Case Reports* **6**, e00369, doi:10.1002/rcr2.369 (2018).

20 Im, J. G. *et al.* Pulmonary tuberculosis: CT findings--early active disease and sequential change with antituberculous therapy. *Radiology* **186**, 653-660, doi:10.1148/radiology.186.3.8430169 (1993).

21 Sundaram, B., Chughtai, A. R. & Kazerooni, E. A. Multidetector high-resolution computed tomography of the lungs: protocols and applications. *Journal of Thoracic Imaging* **25**, 125-141, doi:10.1097/RTI.0b013e3181d9ca37 (2010).

22 Yanagawa, M. *et al.* Multidetector CT of the lung: image quality with garnet-based detectors. *Radiology* **255**, 944-954, doi:10.1148/radiol.10091010 (2010).

23 Reddy, V. P. *et al.* Ferritin H Deficiency in Myeloid Compartments Dysregulates Host Energy Metabolism and Increases Susceptibility to *Mycobacterium tuberculosis* Infection. *Front Immunol* **9**, 860, doi:10.3389/fimmu.2018.00860 (2018).

24 Chinta, K. C. *et al.* Microanatomic Distribution of Myeloid Heme Oxygenase-1 Protects against Free Radical-Mediated Immunopathology in Human Tuberculosis. *Cell Reports* **25**, 1938-1952 e1935, doi:10.1016/j.celrep.2018.10.073 (2018).

25 Dewhirst, M. W., Secomb, T. W., Ong, E. T., Hsu, R. & Gross, J. F. Determination of local oxygen consumption rates in tumors. *Cancer Research* **54**, 3333-3336 (1994).

26 Olive, P. L., Vikse, C. & Trotter, M. J. Measurement of oxygen diffusion distance in tumor cubes using a fluorescent hypoxia probe. *International Journal of Radiation Oncology, Biology, Physics* **22**, 397-402, doi:10.1016/0360-3016(92)90840-e (1992).

27 Thomlinson, R. H. & Gray, L. H. The histological structure of some human lung cancers and the possible implications for radiotherapy. *British Journal of Cancer* **9**, 539-549, doi:10.1038/bjc.1955.55 (1955).

28 Kumar, S. *et al.* Intra-Tumoral Metabolic Zonation and Resultant Phenotypic Diversification Are Dictated by Blood Vessel Proximity. *Cell Metabolism* **30**, 201-211 e206, doi:10.1016/j.cmet.2019.04.003 (2019).

29 Im, J. G., Itoh, H., Lee, K. S. & Han, M. C. CT-pathology correlation of pulmonary tuberculosis. *Crit Rev Diagn Imaging* **36**, 227-285 (1995).

30 Im, J.-G. & Itoh, H. Tree-in-Bud Pattern of Pulmonary Tuberculosis on Thin-Section CT: Pathological Implications. *Korean Journal of Radiology* **19**, 859, doi:10.3348/kjr.2018.19.5.859 (2018).

31 Md. Aejazur Rahman *et al.* Hydrogen sulfide dysregulates the immune response by suppressing glycolysis to exacerbate tuberculosis. *Proc Natl Acad Sci U S A* **117**, 6663-6674, doi:10.1073/pnas.1919211117 (2020).

32 Hunter, R. L. The Pathogenesis of Tuberculosis: The Early Infiltrate of Post-primary (Adult Pulmonary) Tuberculosis: A Distinct Disease Entity. *Front Immunol* **9**, 2108, doi:10.3389/fimmu.2018.02108 (2018).

33 Medlar, E. M. Primary and reinfection tuberculosis as the cause of death in adults; an analysis of 100 consecutive necropsies. *Am Rev Tuberc* **55**, 517-528 (1947).

34 Medlar, E. M. Pathogenetic concepts of tuberculosis. *Am J Med* **9**, 611-622, doi:10.1016/0002-9343(50)90211-7 (1950).

35 Esmail, H. *et al.* Characterization of progressive HIV-associated tuberculosis using 2-deoxy-2-[(18)F]fluoro-D-glucose positron emission and computed tomography. *Nature Medicine* **22**, 1090-1093, doi:10.1038/nm.4161 (2016).

36 Esmail, H. *et al.* Complement pathway gene activation and rising circulating immune complexes characterize early disease in HIV-associated tuberculosis. *Proc Natl Acad Sci U S A* **115**, E964-E973, doi:10.1073/pnas.1711853115 (2018).

37 Diedrich, C. R., O'Hern, J. & Wilkinson, R. J. HIV-1 and the *Mycobacterium tuberculosis* granuloma: A systematic review and meta-analysis. *Tuberculosis (Edinb)* **98**, 62-76, doi:10.1016/j.tube.2016.02.010 (2016).

38 Prideaux, B. *et al.* The association between sterilizing activity and drug distribution into tuberculosis lesions. *Nature Medicine* **21**, 1223-1227, doi:10.1038/nm.3937 (2015).

39 Ordonez, A. A. *et al.* Dynamic imaging in patients with tuberculosis reveals heterogeneous drug exposures in pulmonary lesions. *Nat Med*, doi:10.1038/s41591-020-0770-2 (2020).

40 Braunstein, M., Hickey, A. J. & Ekins, S. Why Wait? The Case for Treating Tuberculosis with Inhaled Drugs. *Pharm Res* **36**, 166, doi:10.1007/s11095-019-2704-6 (2019).

41 De Bouronville, S. *et al.* Exploring Polyoxometalates as Non-Destructive Staining Agents for Contrast-Enhanced Microfocus Computed Tomography of Biological Tissues. *Acta Biomaterialia*, doi:10.1016/j.actbio.2020.01.038 (2020).

42 Waterhouse, D. J., Fitzpatrick, C. R. M., Pogue, B. W., O'Connor, J. P. B. & Bohndiek, S. E. A roadmap for the clinical implementation of optical-imaging biomarkers. *Nat Biomed Eng* **3**, 339-353, doi:10.1038/s41551-019-0392-5 (2019).

# Figure 1

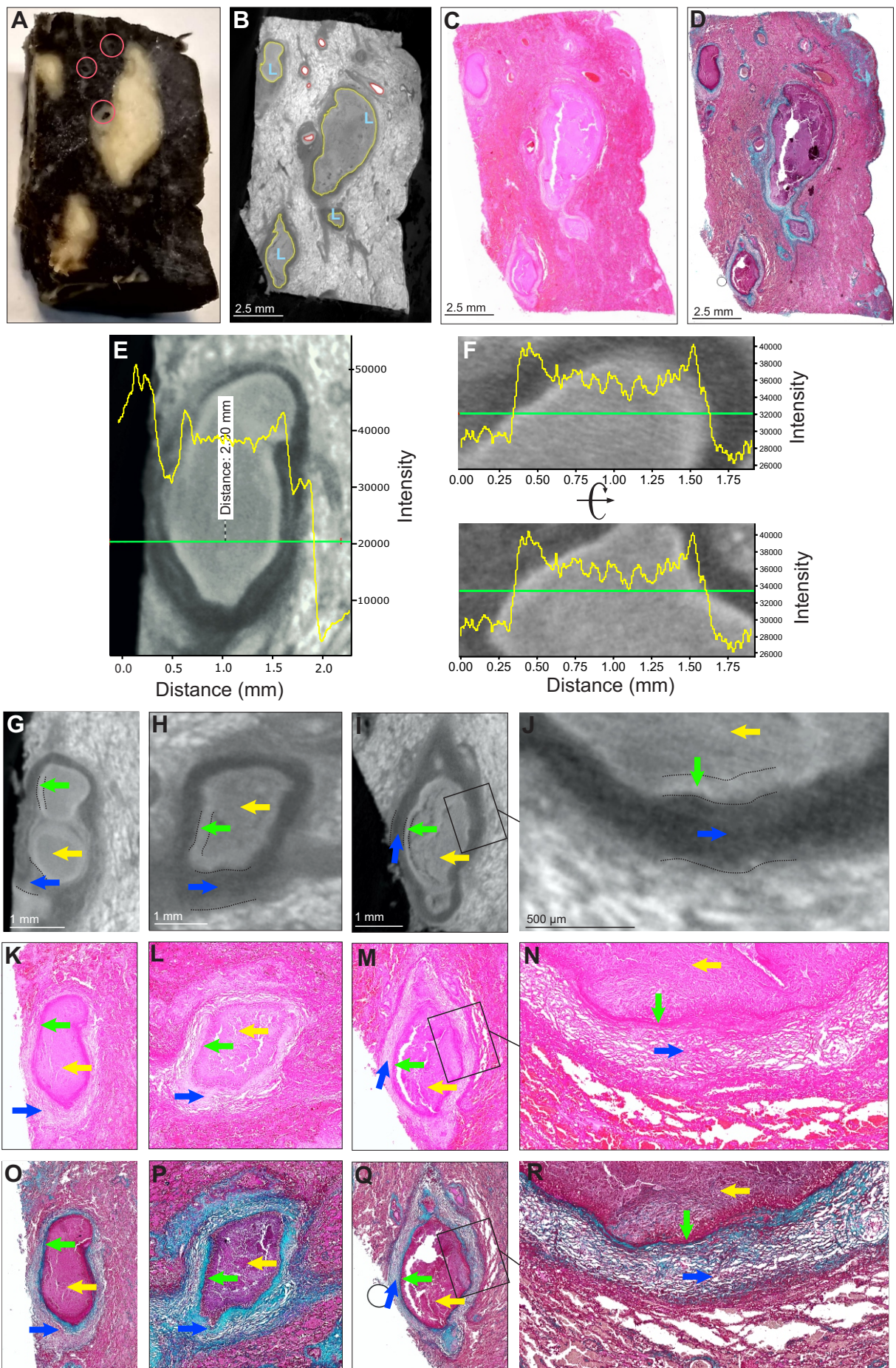
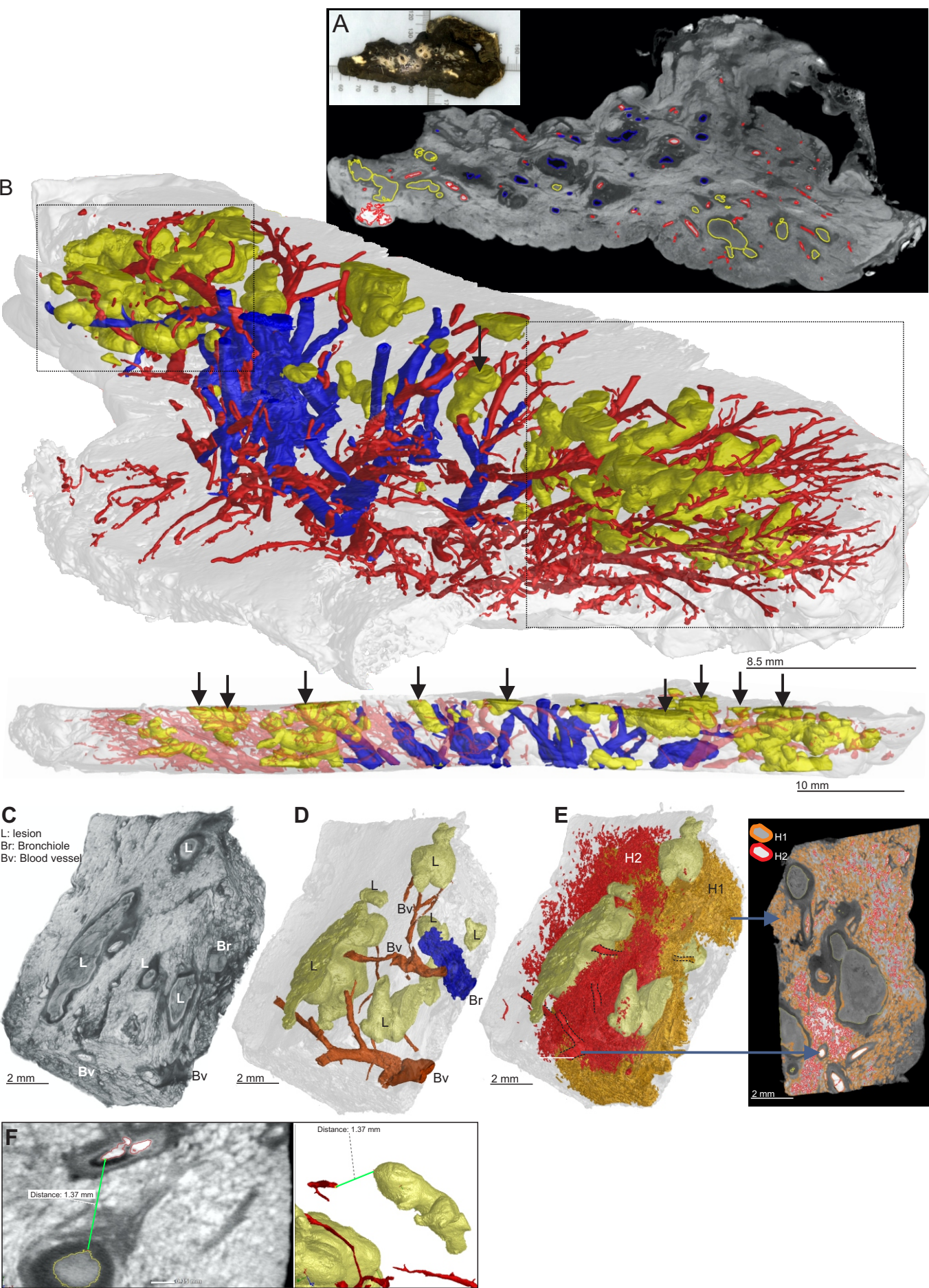
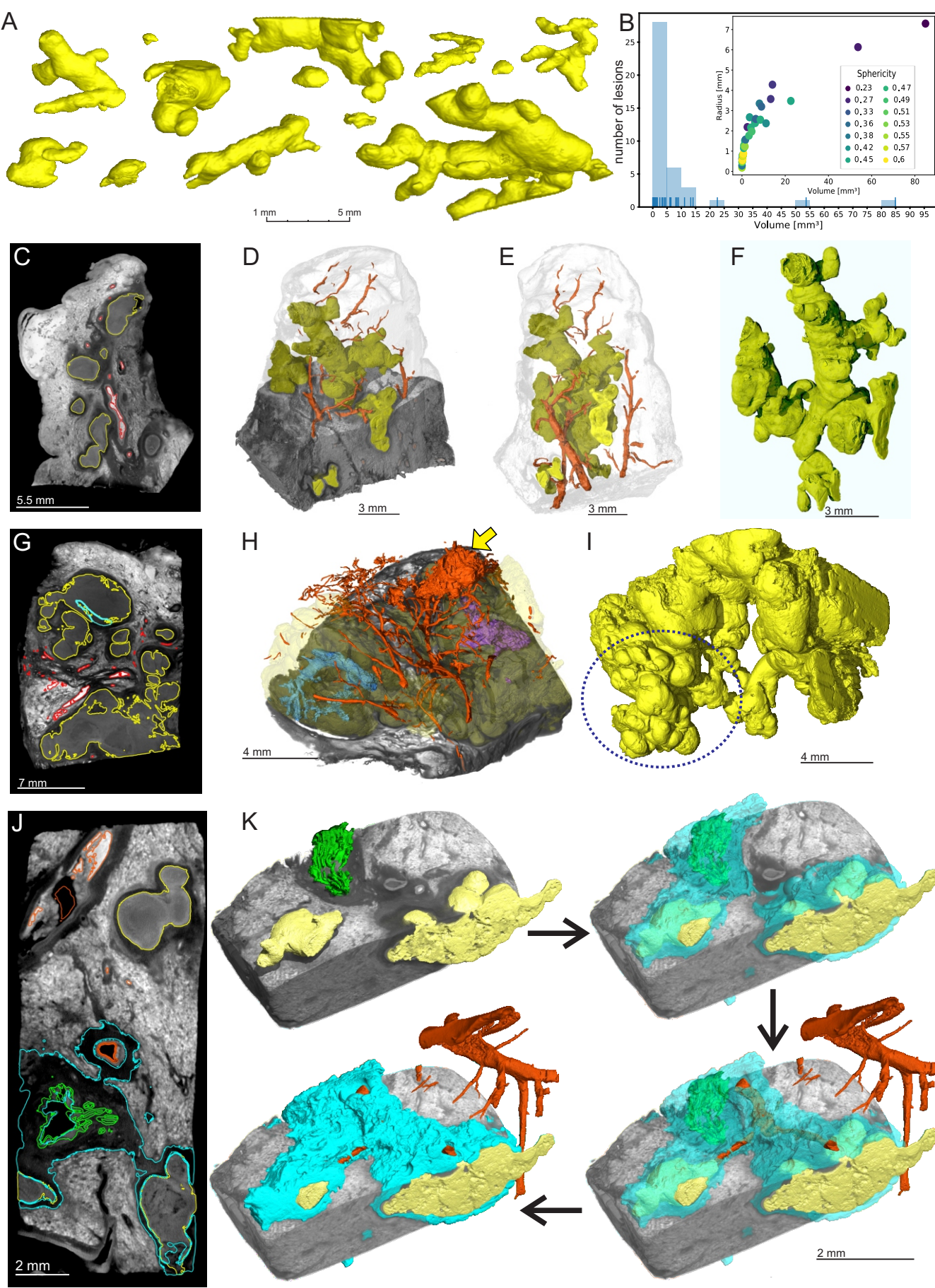


Figure 2



### Figure 3



# Figure 4

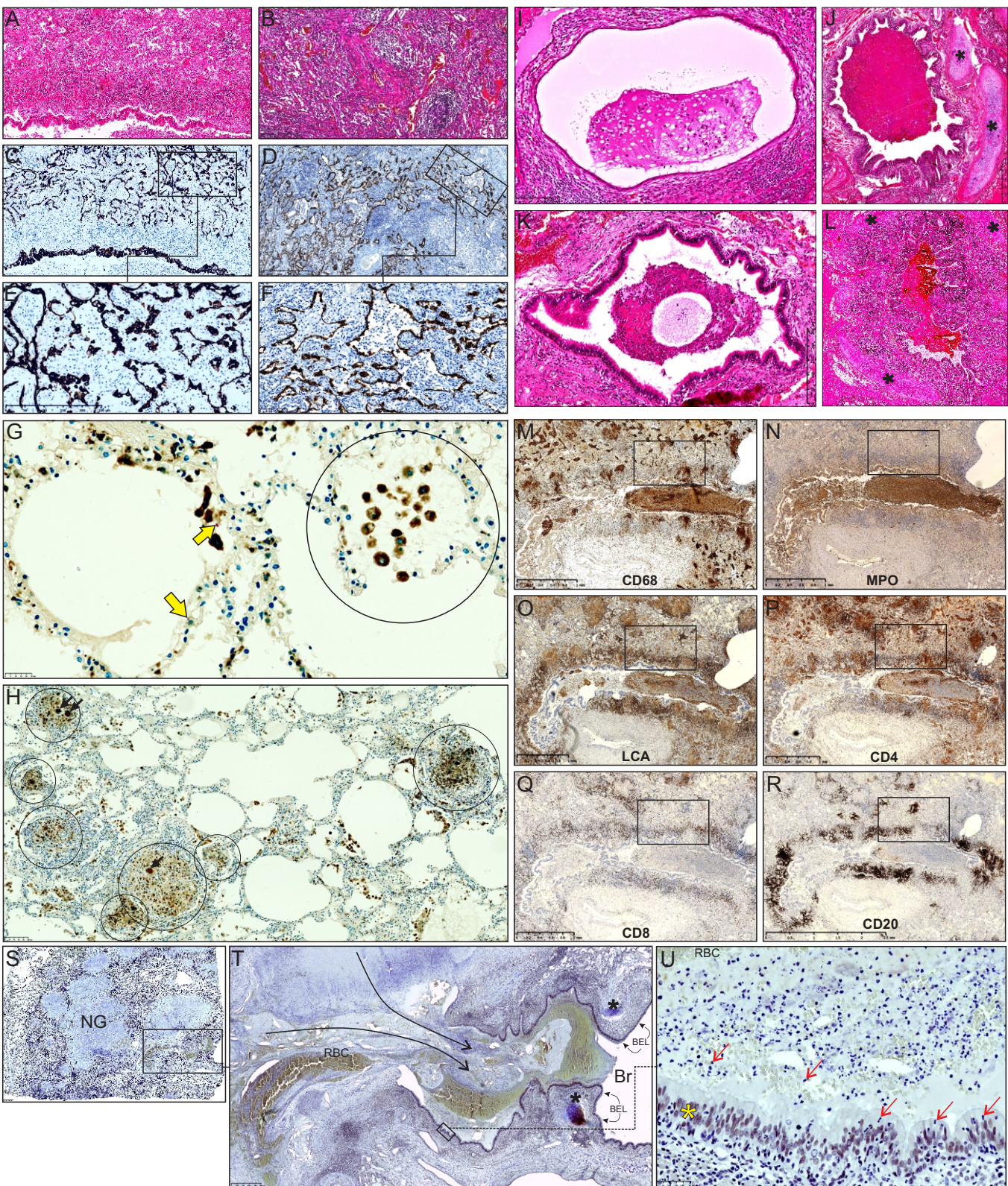


Figure S1



Figure S2

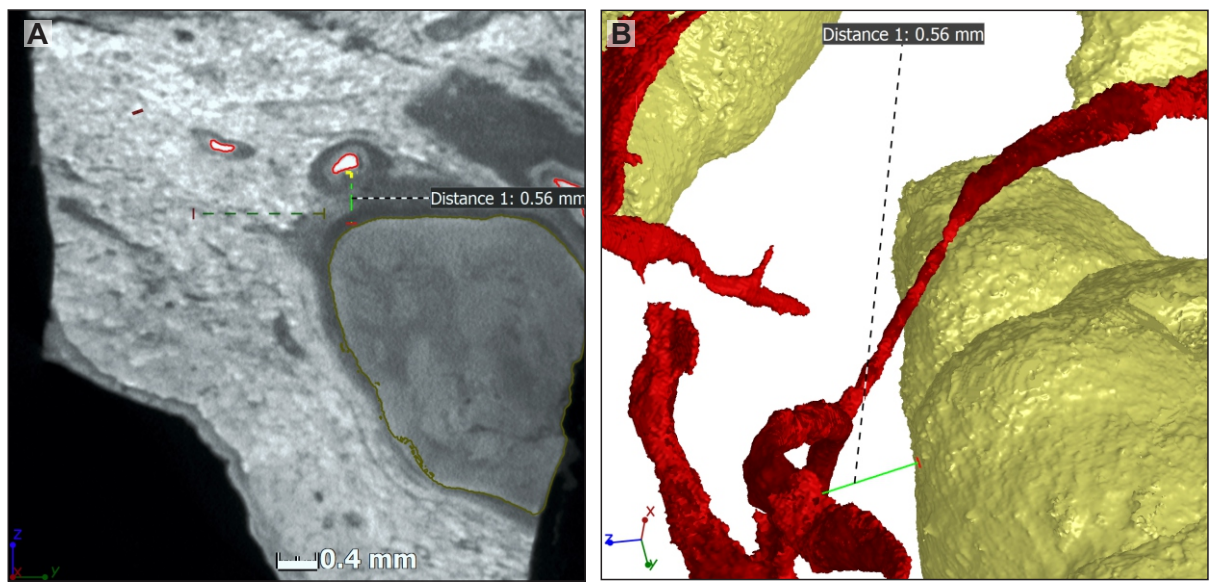


Figure S3A

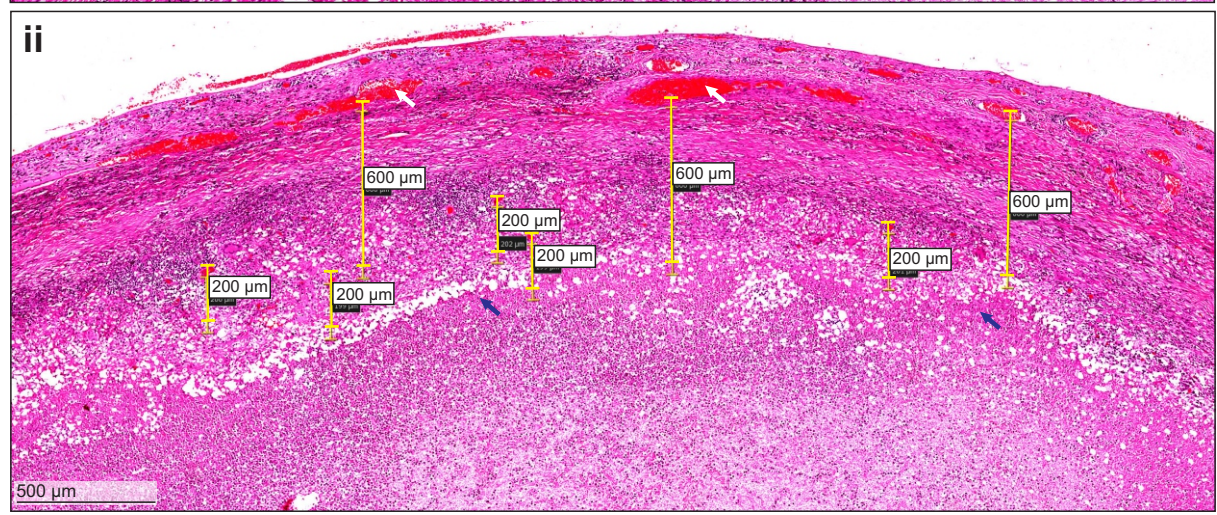
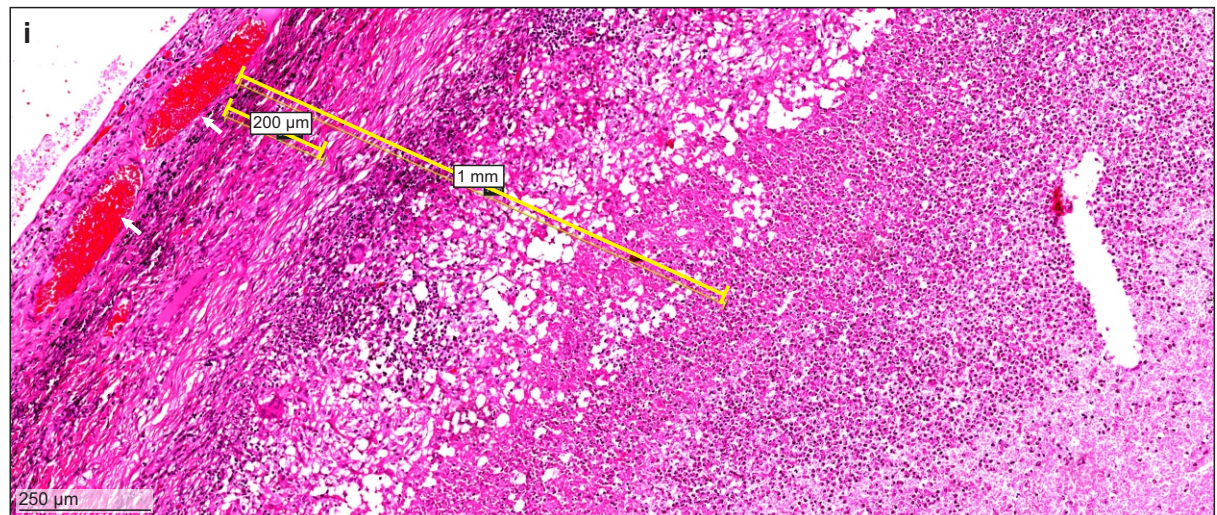
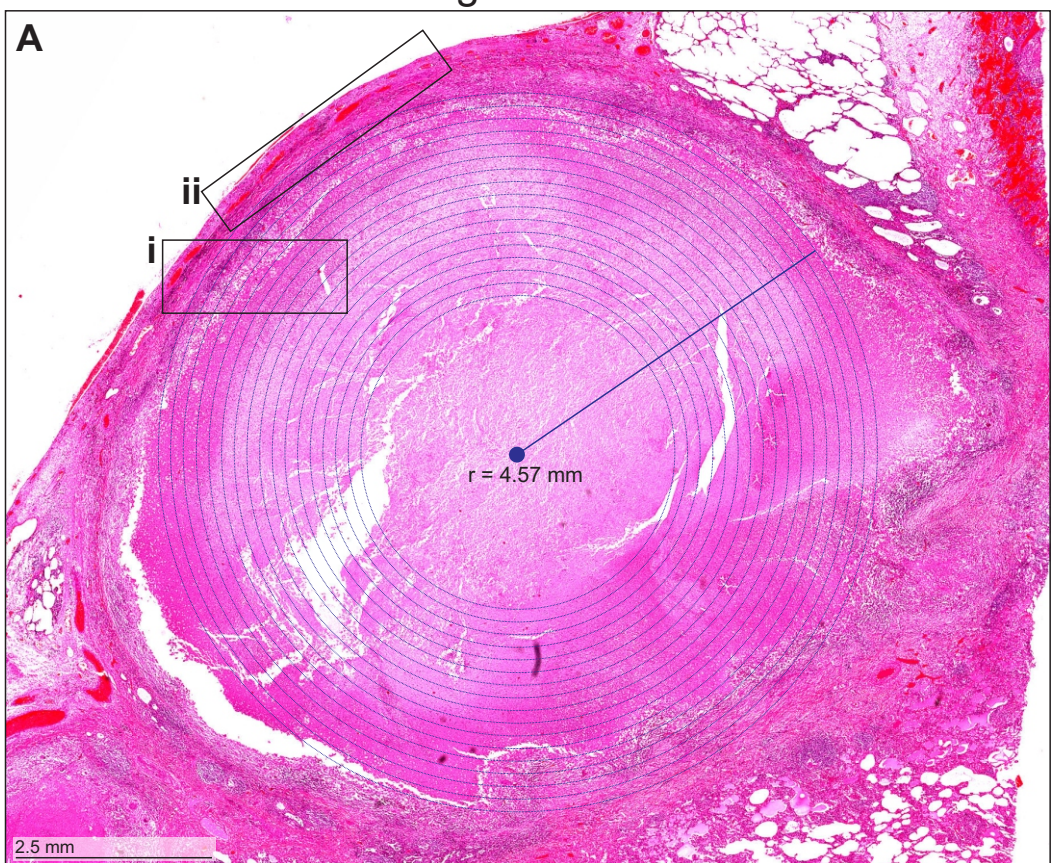


Figure S3B

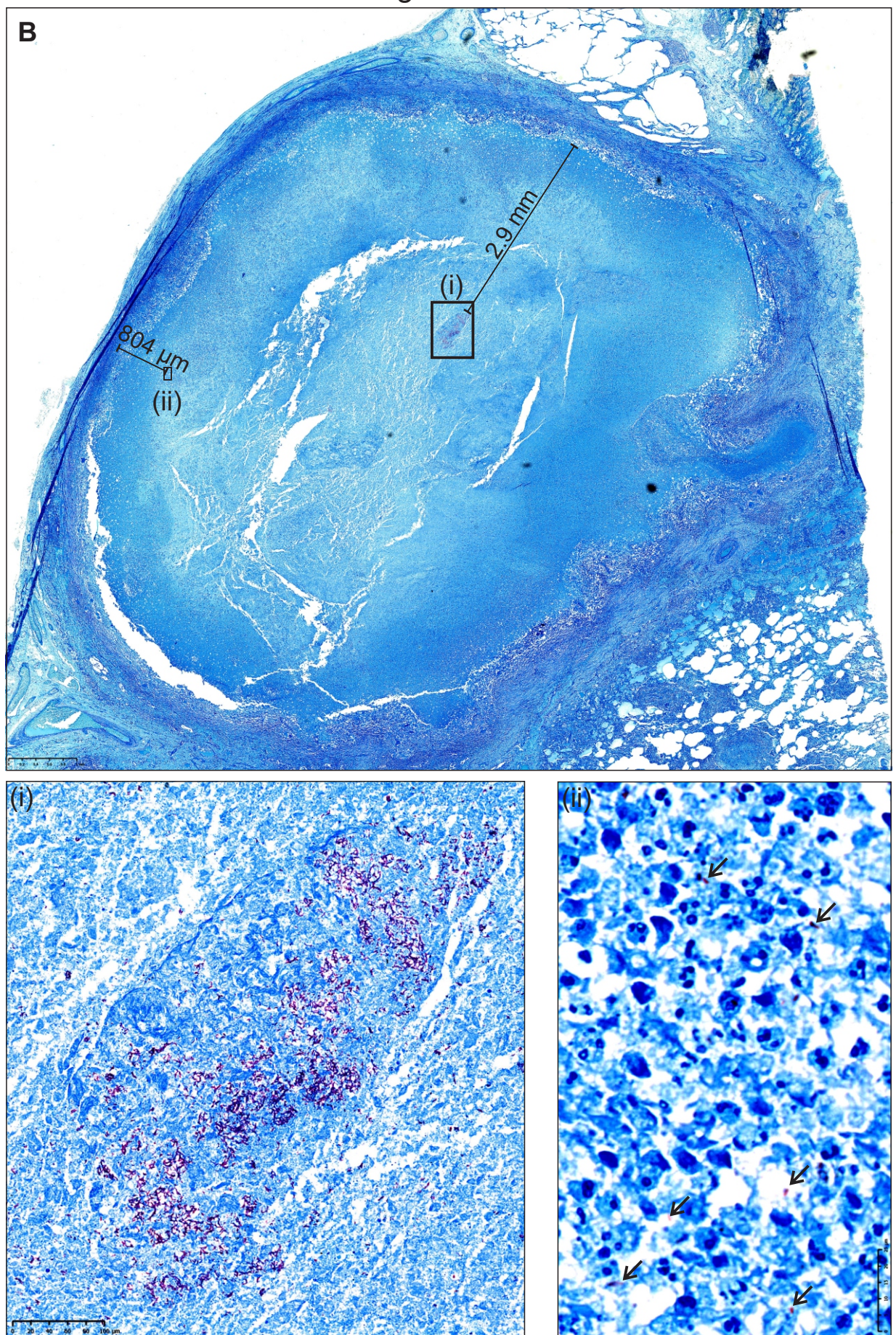


Figure S4

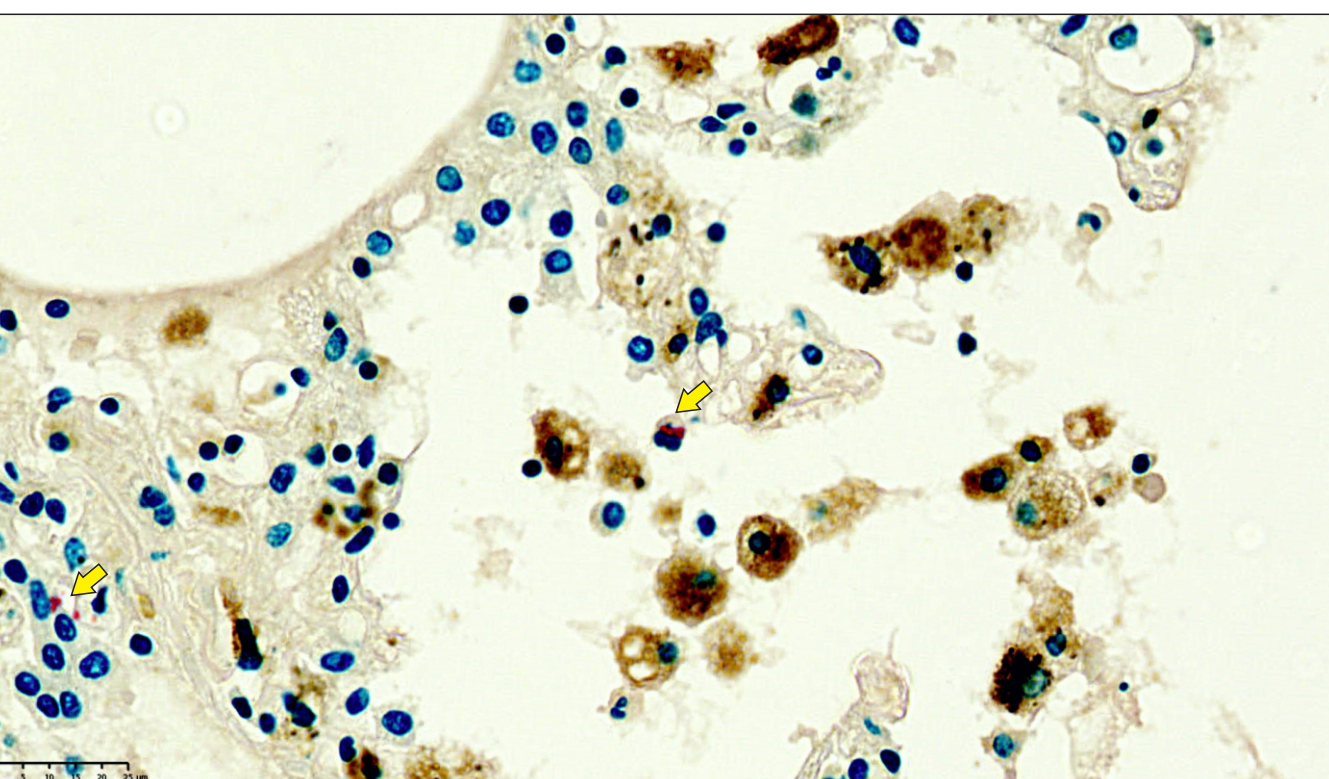


Figure S5

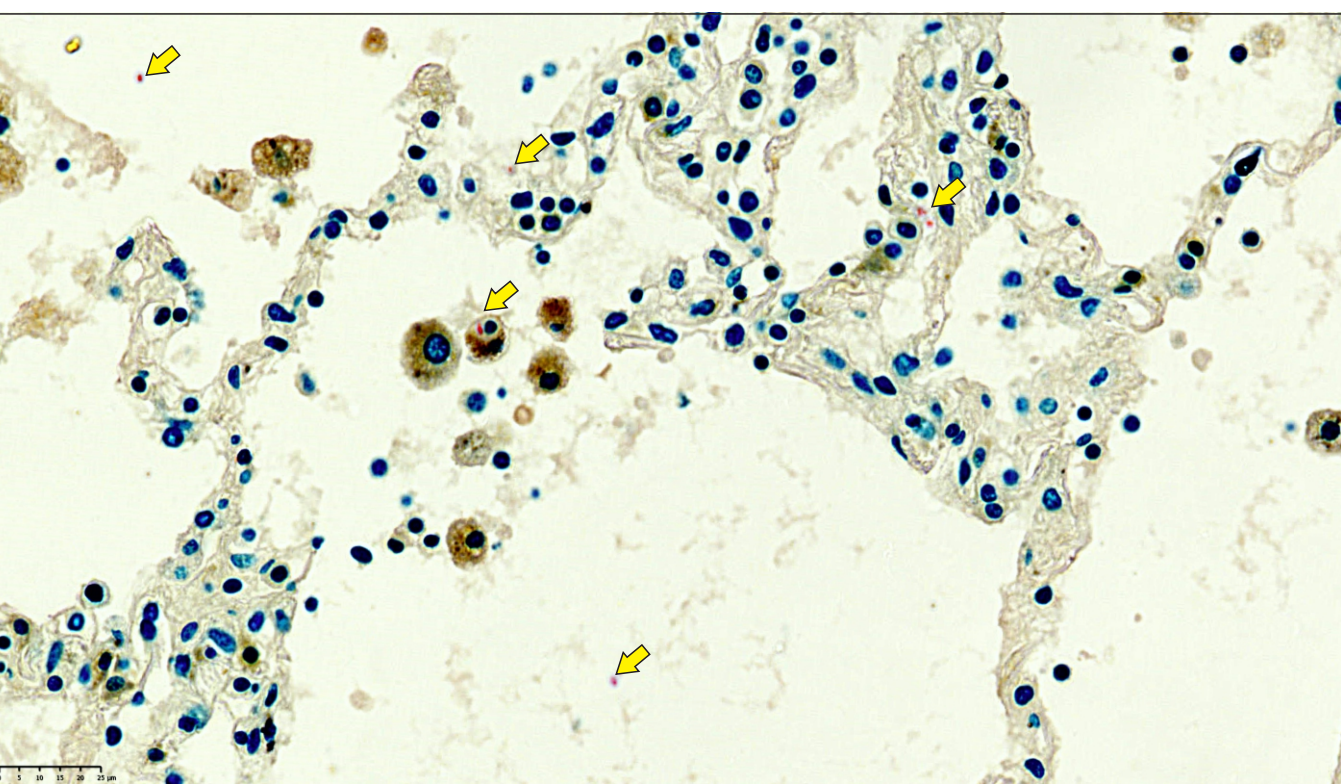


Figure S6

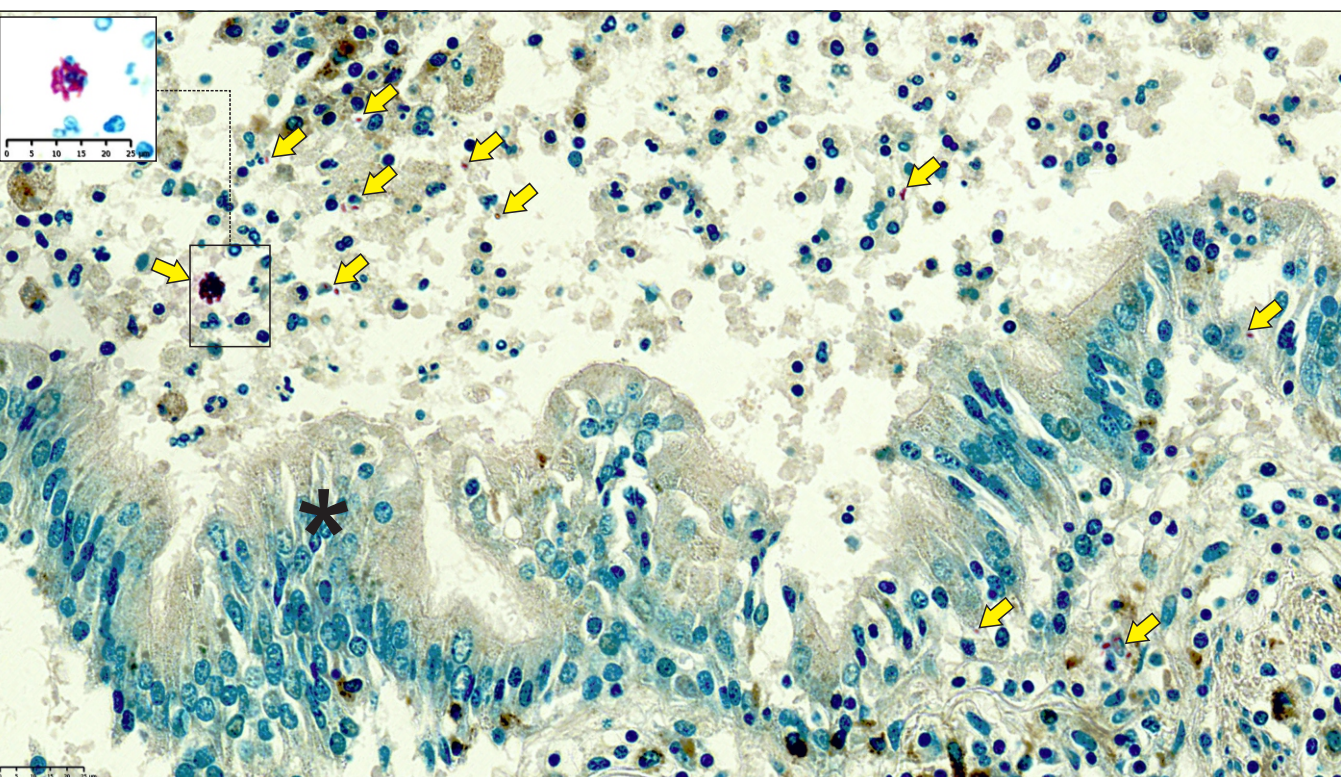


Figure S7

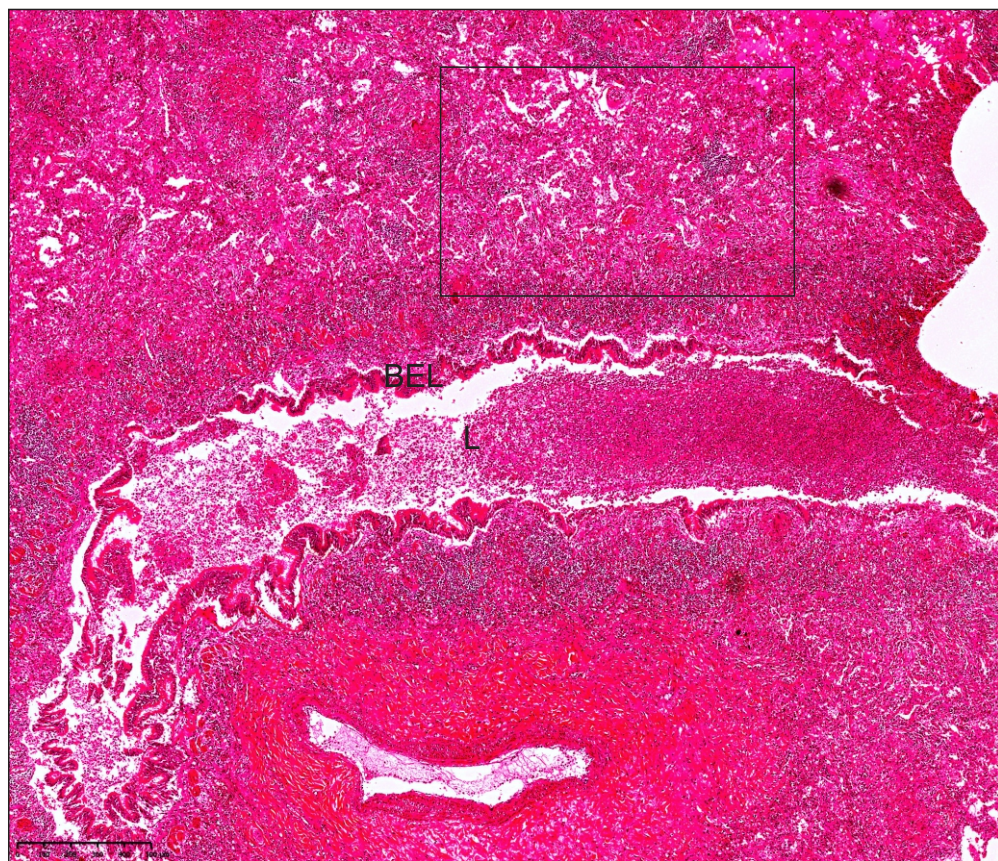


Figure S8

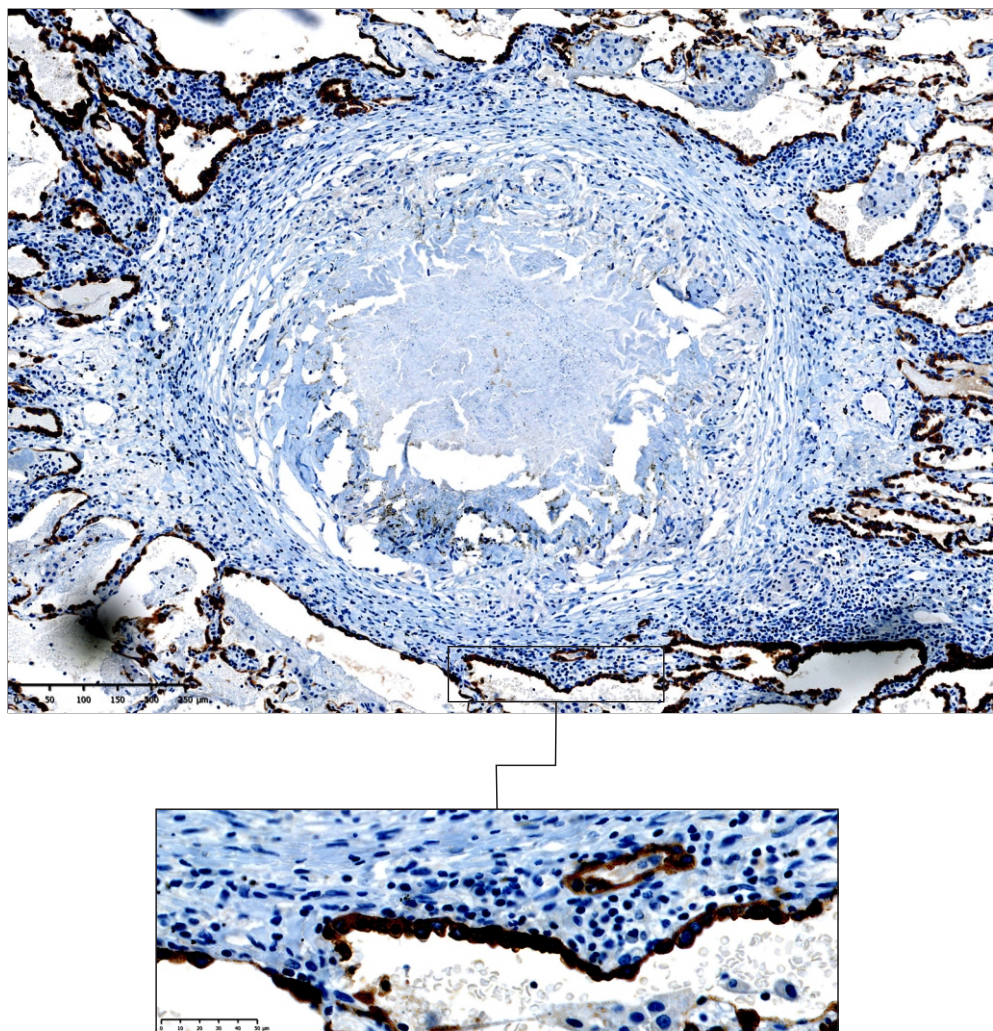


Figure S9

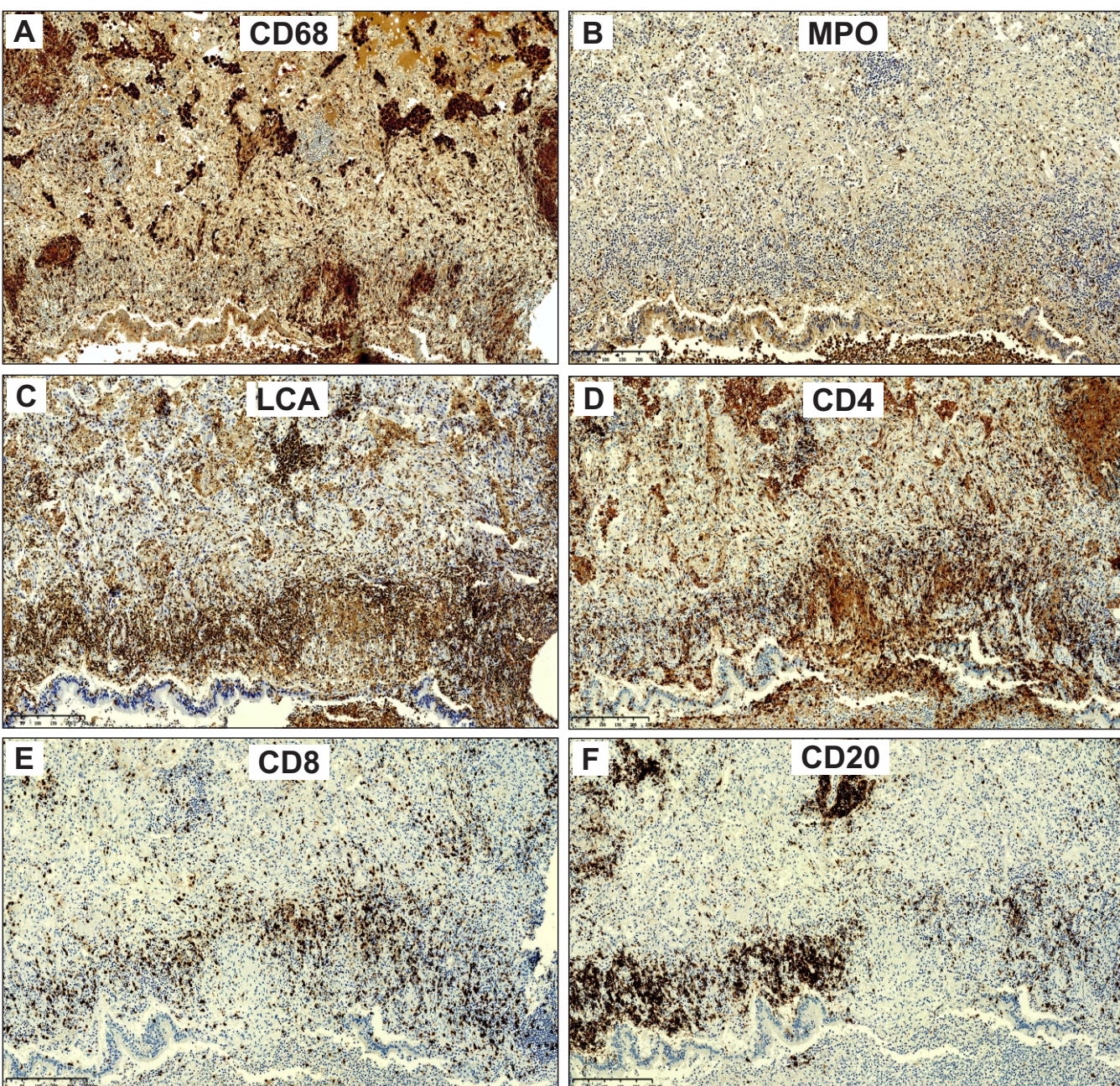


Figure S10

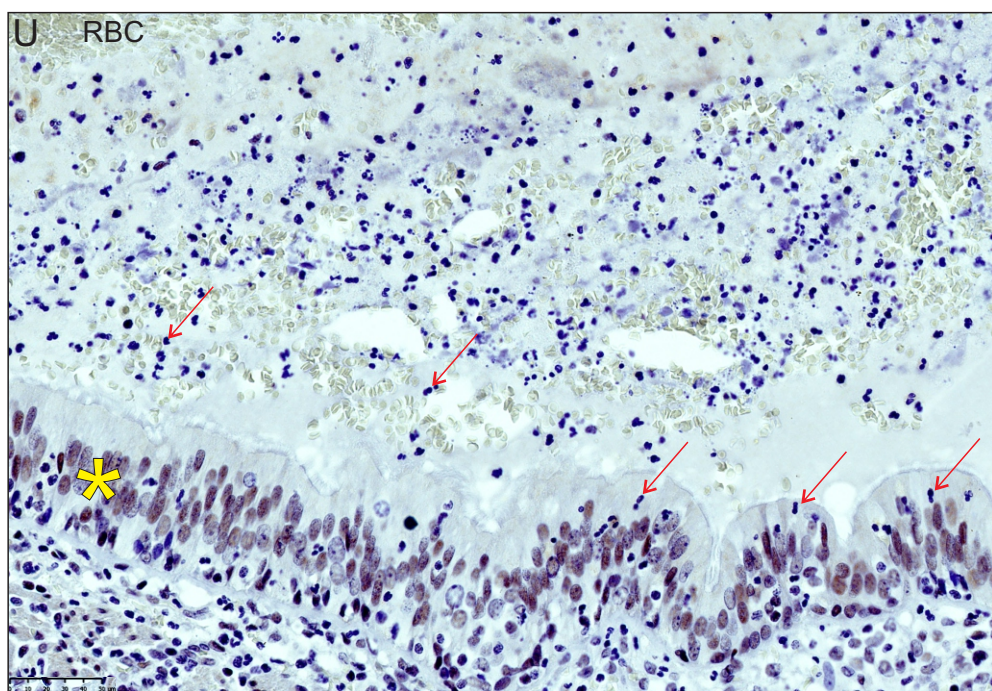
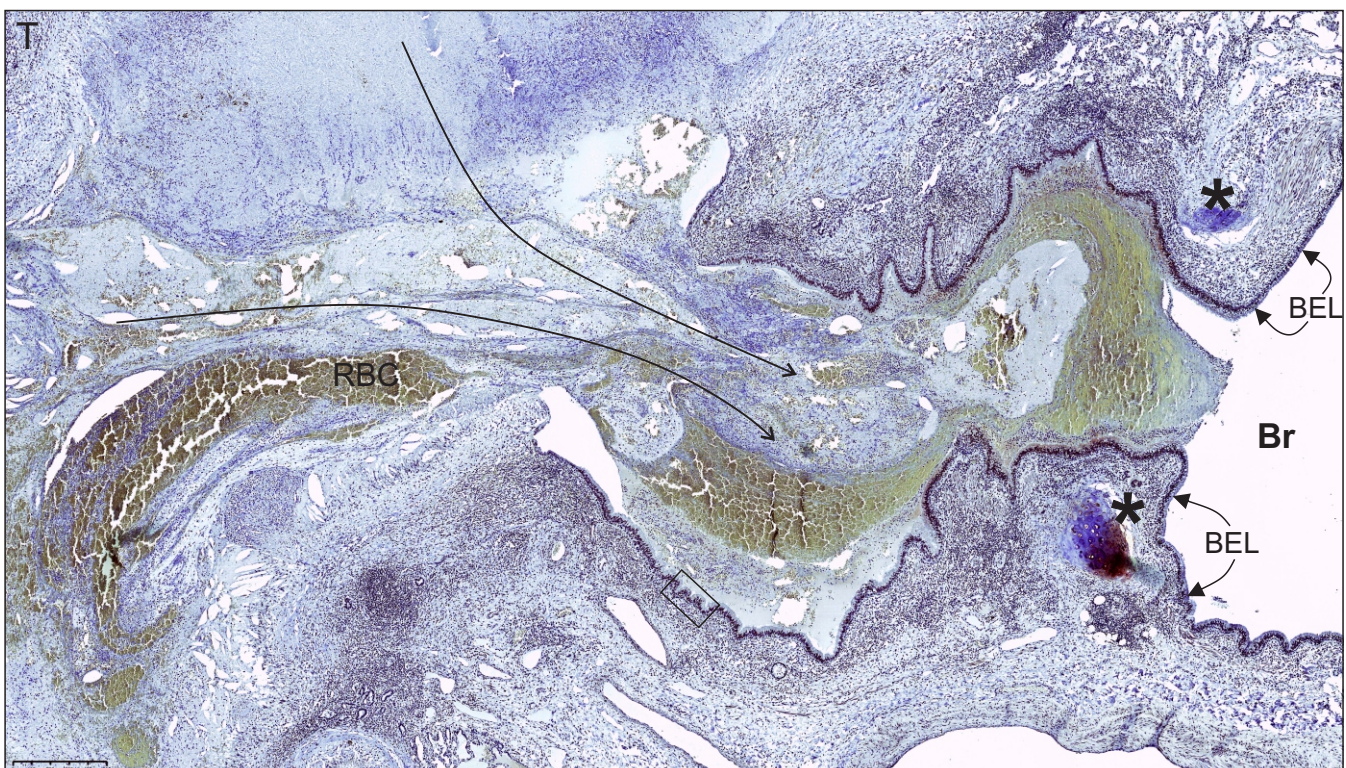
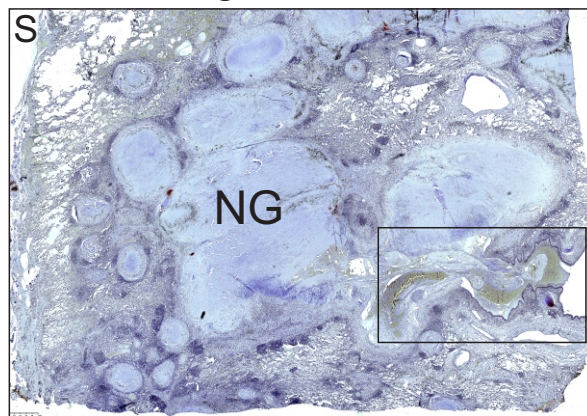


Figure S11

